International Journal of Solids and Structures 308 (2025) 113144

Contents lists available at ScienceDirect

International Journal of Solids and Structures

journal homepage: www.elsevier.com/locate/ijsolstr

Hyperelastic model for nonlinear elastic deformations of graphene-based polymer nanocomposites

Matteo Pelliciari [a,*], Stefano Sirotti [a], Angelo Aloisio [b], Angelo Marcello Tarantino [a]

[a] DIEF, Department of Engineering "Enzo Ferrari", via P. Vivarelli 10, 41125 Modena, Italy
[b] Department of Civil, Construction-Architectural and Environmental Engineering, Università degli Studi dell'Aquila, L'Aquila, 67100, Italy

ARTICLE INFO

Keywords:
Elastomers
Graphene
Experimental mechanics
Hyperelasticity
Nonlinear modeling

ABSTRACT

Graphene-based polymer nanocomposites (PNCs) are increasingly important in engineering applications involving large deformations. However, the nonlinear behavior of these materials has not been thoroughly studied. Current models do not address the specific nonlinear effects of graphene nanofillers under large strains, lack sufficient comparison with experimental data, and primarily focus on uniaxial behavior without exploring biaxial responses, which are relevant in technological applications. This study investigates PNCs composed of silicone elastomer and graphene nanoplatelets (GNPs). We present experimental tests conducted in both simple tension and biaxial inflation on circular membranes. A homogenized hyperelastic model is developed, incorporating distinct contributions from the matrix and the nanofiller. Specifically, we introduce a novel strain energy function for the nanofiller contribution, tailored to reproduce the observed experimental behavior. The model accurately predicts the nonlinear elastic response of the studied PNCs across varying contents of GNPs. The proposed strain energy function is implemented in MATLAB to obtain an exact numerical solution for the inflation of circular PNC membranes. Finally, to demonstrate its broader applicability, the hyperelastic model is applied to additional experimental data from other PNCs found in the literature. This model contributes to establishing a robust framework for the effective use of PNCs.

1. Introduction

Polymers and other rubber-like materials are capable of withstanding large elastic deformations. This is a key feature employed in many engineering applications, such as biomedicine (Guimard et al., 2007), soft robotics (Gorissen et al., 2019; Chen et al., 2019), electronics (Stewart and Sitaraman, 2021; Liu et al., 2021), and impact engineering (Du Bois et al., 2006). However, the high stretchability of polymers comes with relatively low stiffness and strength compared to other technological materials. Additionally, most polymers lack electrical conductivity, which is crucial in devices for flexible electronics (Corzo et al., 2020). Therefore, in the early decades of the 20th century, polymers began to be reinforced by stiff fillers such as silica and carbon black to increase stiffness, strength, and electrical conductivity (Yamaguchi et al., 2003; Lorenz and Klüppel, 2012).

The introduction of nanoparticles, such as carbon nanotubes (CNTs) and graphene nanoplatelets (GNPs), has opened the door to new fillers with significant potential. The material obtained by mixing a polymer matrix with nanoparticles is known as a polymer nanocomposite (PNC). Due to the exceptional mechanical and electrical properties of CNTs and GNPs, as well as their large specific surface area, even a relatively low volume fraction can lead to substantial improvements in the properties of the polymer matrix (Kim et al., 2010; Das et al., 2012; Gao, 2017; Fu et al., 2019). Young et al. (2018) observed that reinforcing the thermoplastic elastomer Alcryn 2265 with 10% by volume of GNPs increased the Young's modulus of the matrix by approximately six times. Mondal and Khastgir (2017) reported a 46% increase in the elastic stiffness of NBR polymer with only 1 part per hundred rubber (phr) of GNP content, and a 247% increase with 15 phr. Qian et al. (2000) found that adding just 1% in weight of CNTs to polystyrene composites resulted in a 25% increase in tensile strength and a 40% increase in elastic stiffness. Electrical and thermal properties are also significantly enhanced. For instance, Winey et al. (2007) reported that the electrical conductivity of polystyrene reinforced with 10% by weight of single-wall CNTs increases from 10^{-5} to 1 S/cm. Wang et al. (2015) observed a 115% improvement in the thermal conductivity of a GNP/epoxy nanocomposite with a content of 5% in weight of nanofiller. In light of these and other exceptional properties, PNCs offer important advantages in various promising applications, including the

* Corresponding author.
E-mail addresses: matteo.pelliciari@unimore.it (M. Pelliciari), stefano.sirotti@unimore.it (S. Sirotti), angelo.aloisio1@univaq.it (A. Aloisio), angelomarcello.tarantino@unimore.it (A.M. Tarantino).

https://doi.org/10.1016/j.ijsolstr.2024.113144
Received 26 August 2024; Received in revised form 5 November 2024; Accepted 11 November 2024
Available online 19 November 2024

development of ultra-stretchable sensors (Qin et al., 2015), coatings for gas barriers (Cui et al., 2016), self-healing materials (Thakur and Kessler, 2015), energy storage (Wang and Zhu, 2011), and membrane technologies (Miculescu et al., 2016; Bassyouni et al., 2019).

Since numerous applications of polymers rely on their ability to undergo large deformations while maintaining an elastic response (Loew et al., 2019; Xu et al., 2019), the literature has extensively focused on modeling their behavior under finite deformations. The most common approach involves developing phenomenological hyperelastic models in nonlinear elasticity, which are particularly effective because they provide relatively straightforward material models. One of the earliest invariant-based hyperelastic models for isotropic materials is the generalized Rivlin model (Rivlin and Saunders, 1951). Following this foundational work, numerous models have been developed, including the Yeoh and Yeoh–Fleming models (Yeoh, 1990; Yeoh and Fleming, 1997), the Gent and Gent-Gent models (Gent, 1996; Pucci and Saccomandi, 2002), the Carroll model (Carroll, 2011), and the Ogden model (Ogden, 1972). These models have been successfully applied to predict the mechanical response of elastomers and polymers filled with carbon black or silica particles. However, when it comes to PNCs, there remains a significant gap in hyperelastic models that can accurately describe their behavior under finite deformations. Specific challenges in modeling PNCs still need to be addressed to develop models that align with experimental data and ensure reliable application.

Incorporating stiff nanofillers such as CNTs and GNPs into polymers typically enhances the initial stiffness of the polymer matrices (Wang et al., 2024; Caliskan and Gulsen, 2023). However, the behavior of PNCs under large deformations remains a complex and unresolved issue. Experimental evidence suggests that initial stiffness enhancements tend to diminish at larger strains due to the debonding of nanofillers from the matrix. Specifically, Frogley et al. (2003) observed that the stiffness enhancement in silicone-based elastomers with single-wall CNTs is lost after 10%–20% strain. Dufresne et al. (2002), Koerner et al. (2005), and Xing et al. (2014) noted a reduction in failure strains and a loss of stiffness enhancement at larger strains. Potts et al. (2013) dispersed thermally exfoliated graphene oxide into natural rubber and discovered that the strain stiffening of the polymer matrix transitions into pseudo-plastic behavior under large stretches. However, some observations contrast with the above findings. Yang et al. (2018) reported an increase in failure strain for low contents of graphene in silicone rubber nanocomposites, which then decreased only for higher contents around 4%–5% by weight. Additionally, they observed improved strain stiffening at large deformations, contrasting with previous studies. Costa et al. (2018) noted a significant increase in failure strain by incorporating 10% by weight of CNTs in an SBS rubber matrix, contrary to other experimental findings. Sadeghpour et al. (2020) did not observe a decrease in failure strain with increasing graphene content in polyvinyl alcohol-graphene oxide nanocomposites. Varol et al. (2017) found that in PNCs, the strain stiffening in large deformations depends on the volume fraction but not on the size of nanofillers. In contrast, the increase in initial stiffness depends on both the volume fraction and the size of nanofillers.

These varying results highlight the complexity of the behavior of PNCs under finite deformations. The primary factor responsible for this complexity is the interface interactions between the matrix and nanofiller, which significantly influence the mechanical behavior of PNCs (Senses and Akcora, 2013; Shen et al., 2014; Molinari et al., 2018). These interactions depend on several factors, including production methods, the type of nanofiller, and curing and post-processing conditions (Jouault et al., 2014; Idumah and Obele, 2021; Choi et al., 2021; Zare, 2016a). Given the numerous factors affecting these interactions and the contradictory nature of empirical observations, there is a clear need to develop modeling approaches that align with experimental data.

Hyperelastic homogenized models that consider the type, content, and effects of nanofillers on the polymer matrix are an effective approach for predicting the response of PNCs under large strains. However, there has been limited focus on this topic, with only a few studies available. Among these, Cantournet et al. (2007) reinforced an elastomer with multi-wall CNTs and proposed a hyperelastic model based on the rule of mixtures to separate the contributions of the matrix and nanofiller. The analyzed PNC reached failure at relatively low strains in simple tension, specifically within the range of 0.8–1.2. Therefore, nonlinear effects under large deformations, such as reduced stiffness enhancement and strain stiffening caused by diminished interactions between CNTs and matrix, were not observed. This allowed the use of a relatively simple constitutive model to describe the contribution of the nanofillers. Shin et al. (2019) and Arash et al. (2019) proposed multiscale homogenization modeling approaches for hyperelastic PNCs by fitting to molecular dynamics simulations. Their studies focused on epoxy nanocomposites and considered only small deformations in simple tension, up to 6%–8%. Islam et al. (2023) developed a multiscale continuum model specific for polymers reinforced with randomly oriented nanofibers. Other authors employed existing hyperelastic models and fitted the parameters to experimental data on PNCs, without distinguishing between the contributions of the matrix and nanofillers (Barghamadi et al., 2021; He et al., 2022).

The above discussion highlights existing limitations in current hyperelastic models. Firstly, there appears to be a lack of models specifically addressing the effects of graphene nanofillers on the response of polymers under large strains. Secondly, there is a deficiency in comparisons and alignments with experimental data. Lastly, the available experiments mainly focus on uniaxial responses, while there is a lack of experimental investigations exploring the biaxial behavior of PNC membranes, which are increasingly significant in several technological applications. Hence, in this work, we consider PNCs produced by mixing GNPs and silicone elastomer and conduct uniaxial experiments in simple tension and biaxial inflation of membranes. Based on these experimental observations, we propose a homogenized hyperelastic model for graphene-based PNCs under large deformations. The proposed model is valid not only for the specific silicone matrix and GNPs considered but also for other cases, as demonstrated by applying the model to additional experimental data available from the literature.

The novel aspects of the present research are outlined as follows. The primary advancement is the development of a new strain energy function for graphene nanoparticles that specifically accounts for their effects in the nonlinear strain regime. In particular, we employ an additive decomposition of the strain energy into separate contributions from the matrix and the nanoparticles. For the nanoparticles, we propose a new function based on the concept of softening hyperelasticity, which captures the debonding of nanoparticles from the matrix occurring at large strains. This debonding reduces the initial reinforcement effect of the particles in the nanocomposite. Additionally, we introduce procedures to calibrate the parameters of the proposed model by computing residual stresses from experimental data. A final aspect is the implementation of an exact numerical solution for the problem of inflated circular PNC membranes using MATLAB. After calibrating the model parameters, we demonstrate that the model accurately reproduces the experimentally observed biaxial behavior. This is significant because the biaxial response of PNCs has not been thoroughly addressed in the literature from both experimental and numerical perspectives. Through these contributions, our work advances the field of mechanics of solids by establishing a solid foundation for modeling the nonlinear elastic behavior of graphene-based PNCs under large deformations.

The paper is organized as follows. In Section 2, we report the experimental tests on PNCs. Section 3 describes the proposed hyperelastic model for graphene-based PNCs. Subsequently, in Sections 4 and 5, we calibrate the model to the experimental data from uniaxial and biaxial inflation tests, respectively. In Section 6, we fit the model to experimental data on other PNCs from the literature to demonstrate its broader applicability. Finally, conclusions are drawn in Section 7.

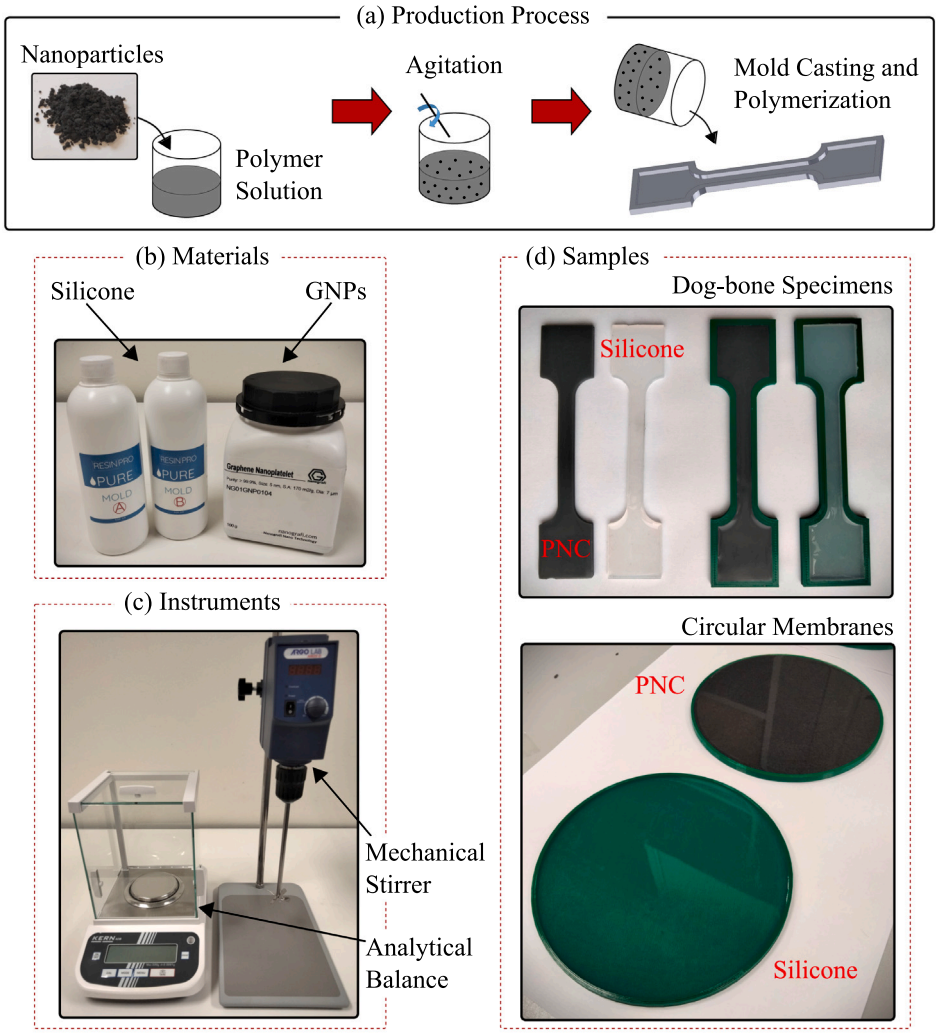

Fig. 1. Scheme of the production of PNCs. (a) GNPs were introduced in the liquid silicone rubber, obtaining a solution that was mixed and then casted into plastic dog-bone-shaped molds and circular molds. Figure (b) shows the silicone matrix and the GNPs. Figure (c) shows the analytical balance and the mechanical stirrer, used to weigh GNPs and agitate the solution, respectively. The obtained dog-bone specimens and circular flat membranes are depicted in figure (d).

2. Experiments

In this section, we describe the production of PNC samples and the subsequent experimental procedures. The conducted experiments encompass simple tension tests and inflation tests on circular flat membranes.

2.1. Samples preparation

For the rubber matrix of the nanocomposites, we employed liquid silicone rubber obtained from RESIN PRO. Specifically, we used Pure Mold liquid silicone rubber with a shore hardness of 13 and a density of 1.1 g/cm^3. This product comprises components A and B, which were mixed at a ratio of 1:1. The working time of this rubber compound is approximately 40 min at 20°, and complete polymerization is achieved after 24 h. As for the nanofiller reinforcement, we utilized GNPs purchased from Nanografi Nano Technology. The GNPs have a declared purity exceeding 99.9%, a density of 2.2 g/cm^3, a size of 5 nm, a diameter of 7 μm, and a specific surface area of 170 m^2/g.

As depicted in Fig. 1(a), to produce PNCs we firstly introduced the nanofiller in the liquid silicone rubber, then the obtained solution was thoroughly mixed. Subsequently, the mixture was cast into dog-bone-shaped molds and circular molds. Figs. 1(b) and (c) respectively show the materials, silicone and GNPs, and the instruments used to weigh the nanofiller and agitate the solution. We used an analytical balance KERN ADB-200-4 with a readability of 0.1 mg to weigh the nanofiller, and a mechanical stirrer AM 20-D ARGOlab to agitate the solution. We measured the nanofiller to obtain solutions with the following GNP contents: 0.2, 0.4, 0.8, 1.4, 2, 4, 6, and 10 phr, which correspond to volume fractions of 0.1%, 0.2%, 0.398%, 0.695%, 0.99%, 1.961%, 2.913%, and 4.762% of the nanocomposite, respectively. The solution was agitated for 15 min at a speed of 600 rpm. Following agitation, the solution was cast into plastic molds to produce dog-bone specimens and circular membranes (Fig. 1(d)). The dog-bone specimens had an effective length of 60 mm, a height of 7 mm, and a thickness of 2.5 mm. The circular membranes had a radius of 60 mm and a thickness of 2.5 mm. Investigation with microscopy revealed good dispersion and random orientation of GNPs within the elastomeric matrix. The images are presented and discussed in Appendix A.1.

2.2. Simple tension test

For each case of PNC with varying GNP content, three dog-bone specimens were tested until failure. Additionally, tests were conducted on the silicone matrix alone. The experiments were carried out using the Instron 5567 testing machine, equipped with a 100 N load cell,

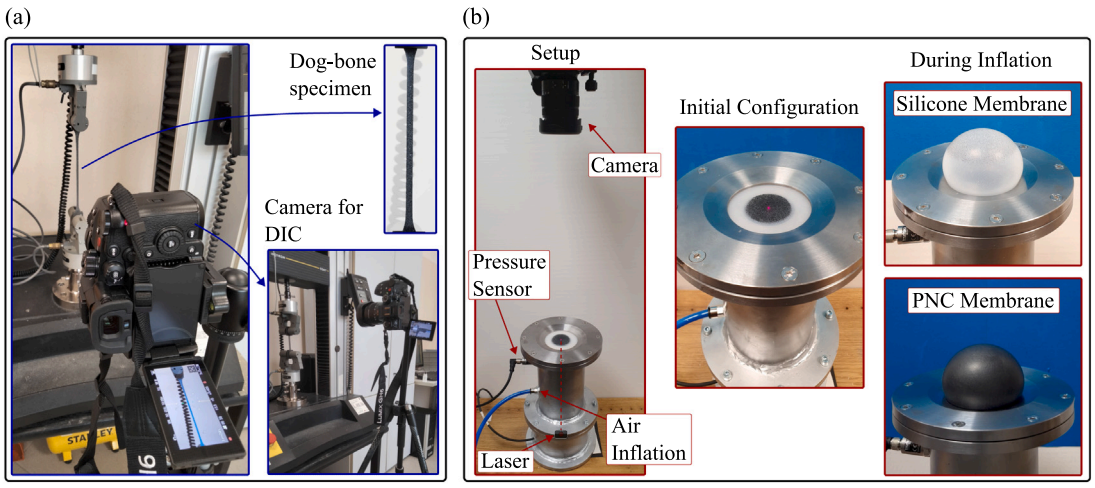

Fig. 2. Experimental tests on PNCs. (a) Simple tension test setup, with a camera positioned in front of the specimen at an orthogonal view for subsequent DIC post-processing. (b) Inflation test conducted on circular flat membranes. The steel tank includes a laser at the bottom to monitor membrane deflection. Air is inflated using an air compressor, with pressure values monitored by a pressure transmitter. A camera positioned orthogonally to the initially flat membrane is used to determine the pole stretch via DIC analysis.

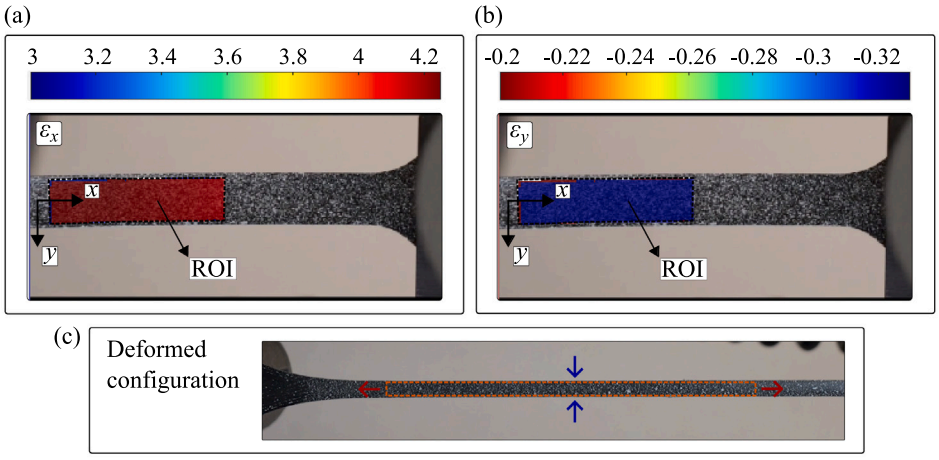

Fig. 3. Results from DIC analysis using MATLAB software *Ncorr* for a specimen with a GNP content of 2 phr. Figures (a) and (b) show respectively longitudinal and lateral Green–Lagrange strains, ε_x and ε_y, at a specific step of the test with $\varepsilon_x = 4.2$. Figure (c) illustrates the deformed configuration, characterized by longitudinal stretching and lateral contraction.

applying elongation at a displacement rate of 120 mm/min. The corresponding strain rate is 0.033 s^{-1}, which is considered quasi-static. Several studies, including those by Meunier et al. (2008), Tomita et al. (2008), and Cheng and Chen (2003), have reported that silicone and common elastomers typically exhibit negligible or minimal strain rate sensitivity within strain rate ranges of approximately 0.005 to 0.1 s^{-1}. Additionally, we note that viscoelastic effects and damage mechanisms may influence the response of elastomers. However, the strain rate used in this study is sufficiently low to minimize such influences, as supported by the literature on quasi-static testing of silicone-based materials.

As depicted in Fig. 2(a), a Panasonic LUMIX DC-GH6 camera was positioned in front of the specimen to record a video of the test from an orthogonal view. Subsequently, the displacement and deformation of the specimen during the test were post-processed using digital image correlation (DIC) with the *Ncorr* package in MATLAB. Further details regarding this can be found in Pelliciari et al. (2023). The Green–Lagrange strains, ε_x and ε_y, in the region of interest (ROI) for a specimen with a GNP content of 2 phr, are displayed in Fig. 3. The variations in their values within the ROI are negligible, indicating homogeneous deformation during simple tension, as expected. The absence of regions with localized strain concentrations confirms the homogeneity of the composites. The same trend was observed in the other samples across the range of GNP contents analyzed.

From the values of the Green–Lagrange strains, the corresponding stretch components were computed as $\lambda_x = \sqrt{1+2\varepsilon_x}$ and $\lambda_y = \sqrt{1+2\varepsilon_y}$. The nominal stress σ_x was computed as F/A, where F is the force applied by the testing machine and A is the cross-section area of the specimen in its initial configuration. For each PNC with a specific GNP content, the variation in results across three tests was minimal. Therefore, we considered the average data of stretches and stresses from the three tests. The obtained experimental curves are presented in Figs. 4(a) and 4(b), depicting σ_x vs. λ_x and λ_y vs. λ_x, respectively.

From Fig. 4(a), it is evident that adding GNPs to the silicone matrix significantly increases the initial stiffness of the nanocomposite. However, as commonly observed in other studies (Frogley et al., 2003; Dufresne et al., 2002; Koerner et al., 2005), an increase in GNP content leads to a decrease in the ultimate stretch. This phenomenon is attributed to particle aggregation and debonding of nanofiller from the matrix during deformation, introducing defects into the material. The decrease in ultimate stretch is relatively limited up to a content of around 2 phr, indicating that nanofiller reinforcement is highly beneficial. However, when the content reaches 4 phr, the ultimate stretch experiences a significant decrease. In fact, the microscopy images presented in Appendix A.1 reveal a gradual increase in particle

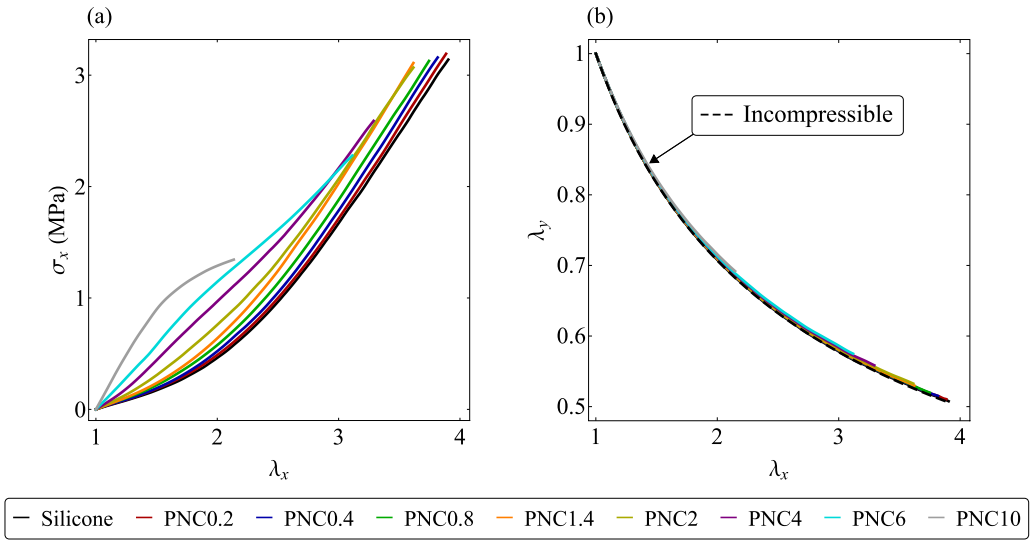

Fig. 4. Experimental curves from simple tension tests. (a) Nominal stress σ_x vs. longitudinal stretch λ_x and (b) lateral stretch λ_y vs. longitudinal stretch λ_x. The black curve represents the data of the silicone matrix alone, while the others depict PNCs with GNP loading reported in the legend in terms of phr (from 0.2 to 10). In figure (b), the dashed black curve shows the behavior of incompressible materials, expressed by $\lambda_y = 1/\sqrt{\lambda_x}$.

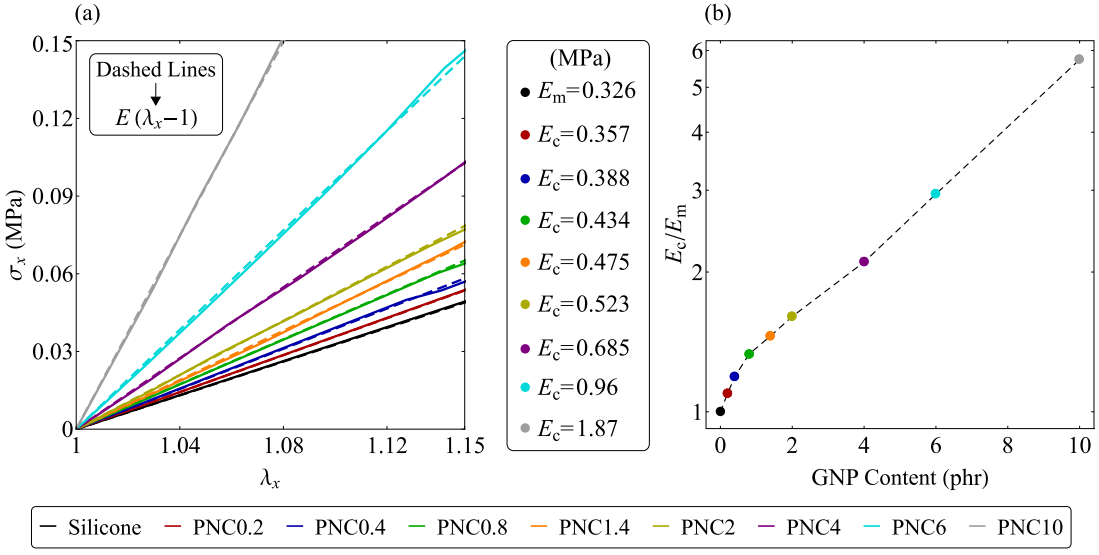

Fig. 5. (a) Experimental data in simple tension for elongation up to 15% (solid lines) and corresponding fitting curves used to estimate the Young's modulus (dashed lines). E_m and E_c represent the Young's modulus of the silicone matrix and PNC, respectively. (b) Semi-logarithmic plot of the ratio E_c/E_m as a function of increasing GNP content.

aggregation with higher GNP content, which subsequently impacts the mechanical performance.

Additionally, the silicone matrix alone exhibits substantial strain stiffening as the stretch increases, particularly beyond a stretch of 2.5. The addition of GNPs reduces the strain stiffening response under large deformations. This reduction is particularly noticeable at a GNP content of 10 phr, where, after reaching a stretch of approximately 1.7, the specimen shows a gradual decrease in stiffness until failure. This behavior has also been reported in other works (see, for instance, Potts et al. (2013)) and is explained by the debonding of the nanofiller from the elastomer matrix under large strains.

The plot in Fig. 4(b) indicates that the introduction of GNPs only minimally affects the response of silicone in terms of longitudinal versus lateral stretches. As expected, the curve representing the silicone matrix (black curve) remains nearly incompressible throughout the test. With increasing GNP content, there is a slight deviation from the incompressible curve (dashed black curve). This deviation is very small and therefore it is reasonable to regard the PNCs as incompressible.

To quantify the increase in elastic stiffness resulting from the presence of GNPs, we analyzed the experimental curves in the small strain region and estimated the values of the elastic modulus. Fig. 5(a) displays the data for elongation up to 15%. In this region, the stress–strain behavior is considered linear, and the data are fitted with the relation $\sigma_x = E(\lambda_x - 1)$, with E representing the estimated Young's modulus. The Young's modulus of the silicone matrix obtained is $E_m = 0.326$ MPa. The increasing values of the modulus E_c of the PNCs with different GNP contents are listed in Fig. 5. A visual representation of the increase in stiffness is presented in Fig. 5(b) through a semi-logarithmic plot of the ratio E_c/E_m as a function of GNP content. With a content of 4 phr, the stiffness more than doubles, and with a content of 10 phr, it increases by almost six times.

2.3. Inflation test on circular membranes

For the inflation test, a handcrafted steel device was built (see Fig. 2(b)). The device comprises a hollow cylinder closed at the bottom

and equipped with a flanged cap at the top, which includes a hole with a 40 mm radius for positioning the circular membrane specimen. The upper flange has a surface knurling with a thickness of 0.1 mm to ensure enhanced adhesion of the membrane compressed between two steel plates.

The device, functioning as a pressure tank, features three openings. At the upper opening, a pressure sensor is mounted to measure the internal pressure of the tank. The pressure transmitter used is the NAH 8254 model from Trafag International, with a measurement range of 0-10 bar and a precision of 0.03 bar. The sensor signal undergoes conversion to pressure values through a current loop operation. The central opening, with a diameter of 5 mm, allows the flow of air supplied by a compressor via a gun equipped with a manometer. The flow is regulated by a screw-type regulator, ensuring quasi-static test execution when nearly closed. Preliminary tests on silicone membranes were conducted to adjust the air flow regulation, achieving a test duration of approximately 70–80 s, which is comparable to that of the simple tension tests (around 100 s). Lastly, the bottom opening transmits the signal of a laser sensor optoNCDT ILD1420-500 from Microepsilon, featuring a measurement range from 100 to 600 mm with an accuracy of 0.01 mm. The laser is directed at the central point of the membrane (pole), and its orthogonality is carefully checked to ensure precise readings. During inflation, the laser signal provides data on the displacement of the membrane pole, thus the membrane deflection.

The two signals from the laser and pressure sensors are acquired by a data acquisition system based on PXI (PCI eXtensions for Instrumentation) hardware and LabVIEW software produced by National Instruments. This system comprises a PXI Chassis housing all necessary hardware modules and providing mechanical, electrical, and communication interfaces. LabVIEW software is used to design the user interface, implement data processing, and control the pressure–deflection curve in real time. The same data acquisition system is employed to acquire both signals, ensuring synchronization. The sampling rate is set at 10 kHz to capture any potential instability phenomena that might occur during quasi-static inflation.

In addition to the setup described previously, as depicted in Fig. 2(b), a camera was installed above the membrane, aligned orthogonally to the initially flat membrane. With this camera, we recorded a video of the experiment and then performed DIC post-processing using the *Ncorr* package in MATLAB. Since the membrane does not remain flat during inflation, it is not feasible to reconstruct the entire three-dimensional deformed geometry with a single camera. However, this is not the purpose of the test or of this work. Our focus is solely on the pole stretch of the membrane, to derive pressure vs. pole stretch data in addition to the pressure vs. deflection data. The computation of pole stretch with DIC analysis is detailed in Appendix A.2.

Two tests were conducted for both the silicone membrane and each of the PNC membranes with varying GNP content. The data of the two tests revealed minimal differences and therefore we consider the average of the two tests. The resulting pressure vs. deflection curves are depicted in Fig. 6(a). The curves are displayed in terms of normalized pressure $\bar{p} = pR/H$ and normalized deflection $\bar{\delta} = \delta/R$, where $H = 2.5$ mm and $R = 40$ mm are membrane thickness and radius, respectively. As the GNP content increases, we observe a trend similar to that seen in simple tension. The stiffness of the response significantly increases, particularly noticeable with contents exceeding 2 phr. Moreover, the ultimate deflection gradually decreases, consistent with the reduction in ultimate stretch due to the increasing presence of defects. The ultimate pressure value increases with GNP content, showing a maximum increase of 36% in the case of 10 phr compared to the silicone matrix.

A remark concerns the phenomenon of limit-point instability, commonly observed in elastomeric membranes. Towards the end of the experiment, we note a significant and abrupt decrease in stiffness in the curves, accompanied by a rapid increase in deflection while pressure remains nearly constant. In the silicone membrane (black curve), we observed this instability during the test, but it only occurred when the membrane was already close to failure. As soon as it occurred, the membrane abruptly reached failure. With increasing GNP content, instability in the PNC membranes tended to disappear. This is attributed to a stiffer response and a decrease in ultimate deflection. Regardless of the GNP content, material failure consistently aligned closely with the limit point instability. This phenomenon is significant for membrane design in practical applications requiring stability and controlled deformations, e.g. biomedical devices and soft robotics.

The pressure vs. pole stretch curves of the membranes are shown in Fig. 6(b). They reflect a similar trend to the pressure vs. deflection data, emphasizing the abrupt decrease in stiffness towards the end of the experiment, suggesting that instability is imminent. Our main aim in measuring pole stretch with DIC was to observe when the membranes reached failure. Remarkably, we found a strong correspondence between the ultimate stretches observed during inflation and those in simple tension tests (Fig. 4). It is interesting to note that typically, one might expect the ultimate stretch during inflation to be smaller than in simple tension due to the biaxial stress state. However, the results suggest that, in a biaxial stress state like inflation, the membrane reaches failure when the stretch approaches approximately the same value observed in simple tension tests.

3. Hyperelastic model for polymer nanocomposites

In this section, we present the phenomenological hyperelastic model for PNCs. Elastomers are generally assumed to be isotropic. Since the nanofiller is randomly oriented, we assume that the PNC maintains the isotropic property of the matrix. Using a homogenized modeling approach, we describe the constitutive behavior of the nanocomposite through the definition of a strain energy (SE) function W. We introduce the deformation gradient $\mathbf{F}$ and the left and right Cauchy–Green deformation tensors, defined as $\mathbf{B} = \mathbf{F}\mathbf{F}^T$ and $\mathbf{C} = \mathbf{F}^T\mathbf{F}$, respectively. For isotropic materials, W is a function of the principal invariants of $\mathbf{B}$, defined as

$$I_1 = \mathrm{tr}\mathbf{B} = \lambda_1^2 + \lambda_2^2 + \lambda_3^2, \quad I_2 = \frac{1}{2}\left[(\mathrm{tr}\mathbf{B})^2 - \mathrm{tr}\left(\mathbf{B}^2\right)\right] = \lambda_1^2\lambda_2^2 + \lambda_1^2\lambda_3^2 + \lambda_2^2\lambda_3^2,$$
$$I_3 = \det\mathbf{B} = \lambda_1^2\lambda_2^2\lambda_3^2, \tag{1}$$

where λ_1, λ_2, and λ_3 are the principal stretches. For incompressible materials, the deformation is isochoric, meaning $I_3 = 1$, and the SE function becomes solely dependent on I_1 and I_2, expressed as $W = W(I_1, I_2)$. This assumption is considered in this work, supported by the experimental curves in simple tension from Fig. 4(b), which show that the PNCs analyzed are nearly incompressible.

The nanofiller content in PNCs is low to modest, so it is assumed that the nanoparticles deform following the deformation of the elastomer matrix. Therefore, the strain energy of the polymer nanocomposite can be viewed as an additive composition of two contributions: one from the elastomer matrix and the other from the nanofiller. Thus, we express the strain energy function using the rule of mixtures as

$$W = (1 - f)W_m + fW_n, \tag{2}$$

where W_m and W_n are the strain energy functions accounting for the matrix and nanofiller contributions, respectively, and f is the volume fraction of nanofiller. A similar approach has also been employed for PNCs by other researchers, particularly in Refs. Cantournet et al. (2007), Islam et al. (2023). The advantage of this method is that the response of the elastomer is calibrated independently. Subsequently, the contribution of the nanofiller is calibrated on a phenomenological basis using experimental data from PNCs with various GNP contents. Note that, as observed in the experiments presented in Section 2, the detachment of nanoparticles from the matrix occurs in PNCs at large strains, affecting the enhancement of material properties. This effect

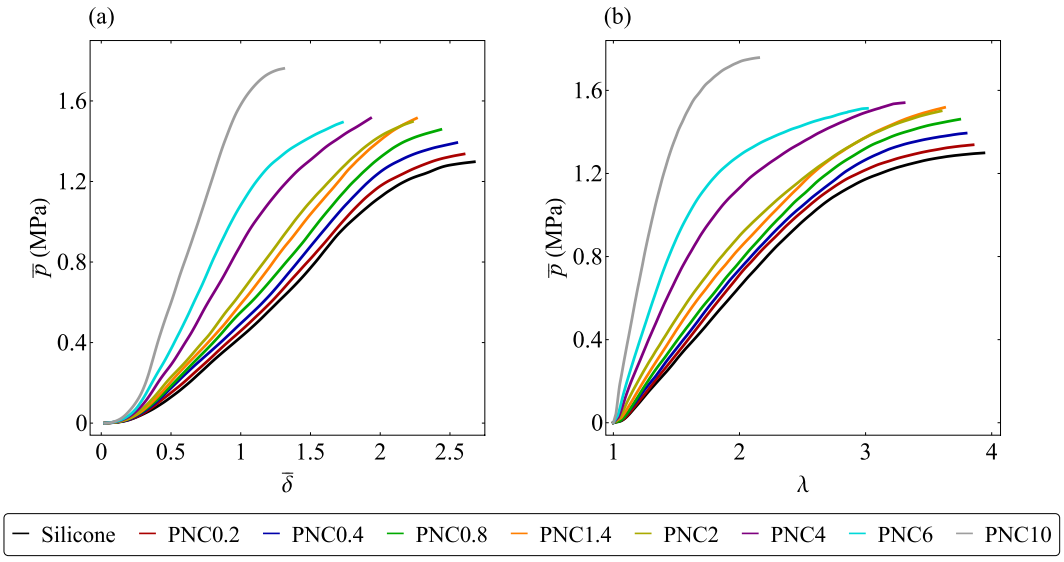

Fig. 6. Experimental curves from biaxial inflation tests on circular membranes. (a) Normalized pressure $\bar{p}$ vs. deflection $\bar{\delta}$ and (b) normalized pressure $\bar{p}$ vs. pole stretch λ. Normalization of pressure and deflection are done by defining $\bar{p} = pR/H$ and $\bar{\delta} = \delta/R$, respectively. The black curve represents the data of the silicone matrix alone, while the others depict PNCs with GNP content reported in the legend in terms of phr.

is incorporated into the nanofiller contribution W_n to the total strain energy, as will be explained in detail in Section 3.2.

We remark that, for general composite materials, reinforcing particles or fibers may exhibit preferred orientations. A widely adopted approach in hyperelasticity, developed by Holzapfel et al. (2000) for composites with fibers aligned in a particular direction, introduces an additional invariant to account for anisotropy due to fiber orientation. This model was later extended by Gasser et al. (2006) to composites with fibers distributed across multiple orientations, using a generalized structure tensor **H**. This approach expresses the SE function contribution of reinforcing fibers in terms of I_4, which captures fiber orientation dispersion. For randomly oriented fibers, the material response becomes isotropic, and I_4 simplifies to $I_1/3$, representing an equivalent isotropic strain measure. Following this framework and given that we are dealing with randomly oriented nanoplatelets, we adopt $I_1/3$ as the strain measure for the nanofiller contribution in our model. Accordingly, we express the SE functions of the matrix and nanoparticles as $W_m = W_m(I_1, I_2)$ and $W_n = W_n(I_1)$.

The Cauchy stress tensor **T** of the nanocomposite is given by

$$\mathbf{T} = \frac{\partial W}{\partial \mathbf{F}}\mathbf{F}^T - p\mathbf{I}, \tag{3}$$

where p denotes the arbitrary hydrostatic pressure associated with the incompressibility constraint. We separate the contributions of the elastomer matrix and nanofiller as

$$\mathbf{T}_m = \frac{\partial W_m}{\partial \mathbf{F}}\mathbf{F}^T - p_m\mathbf{I}, \quad \mathbf{T}_n = \frac{\partial W_n}{\partial \mathbf{F}}\mathbf{F}^T - p_n\mathbf{I}, \tag{4}$$

with $p = (1-f)p_m + f p_n$. Thus, the Cauchy stress of the nanocomposite is obtained additively as $\mathbf{T} = (1-f)\mathbf{T}_m + f\mathbf{T}_n$. Accordingly, the first Piola–Kirchhoff stress tensor $\mathbf{P} = \mathbf{T}\mathbf{F}^{-T}$ is decomposed additively in the two contributions of matrix and nanofiller as

$$\mathbf{P} = (1-f)\mathbf{P}_m + f\mathbf{P}_n, \tag{5}$$

where

$$\mathbf{P}_m = \mathbf{T}_m\mathbf{F}^{-T}, \quad \mathbf{P}_n = \mathbf{T}_n\mathbf{F}^{-T}. \tag{6}$$

3.1. Strain energy of polymer matrix

The silicone matrix exhibits typical elastomeric behavior, characterized by strain stiffening resulting from the alignment and stretching of polymer chains. Numerous hyperelastic models in the literature describe such behavior, with one common choice being the Yeoh–Fleming model (Yeoh and Fleming, 1997). The SE function of this model is expressed as

$$W_m = \frac{A}{B}\left(1 - e^{-B(I_1-3)}\right) - C_{10}\left(I_m - 3\right)\ln\left(1 - \frac{I_1 - 3}{I_m - 3}\right), \tag{7}$$

where A, B, C_{10}, and I_m are material constants. This function was specifically developed by combining concepts proposed by Yeoh and Gent to optimize behavior at both small and large strains. The exponential term, involving A and B, governs the behavior at small strains and was derived by observing the trend of shear modulus from experiments. The logarithmic term, involving C_{10} and I_m, governs the response at large strains, with I_m representing the limiting value of I_1 corresponding to the deformation when the polymer chain is fully stretched.

In Pelliciari et al. (2023), the authors analyzed elastomers with characteristics similar to the silicone considered in this work. They compared different hyperelastic models and found that, for the materials analyzed, the most effective in terms of the number of parameters and quality of fitting was the Yeoh–Fleming model. Therefore, we chose this model for the silicone matrix. Note that other hyperelastic models could also be suitable. The additive decomposition of the SE function of Eq. (2) allows for the selection of a different strain energy function for the matrix if deemed a better choice.

The Cauchy stress tensor of the elastomer matrix is computed by substituting Eq. (7) into Eq. (4), and the Piola–Kirchhoff stress tensor from Eq. (6). For the uniaxial stress state, the nominal stress–stretch relation of the elastomer matrix is given by

$$\sigma_{x,m} = 2\left(1 - \frac{1}{\lambda_x^3}\right)\left(\lambda_x\frac{\partial W_m}{\partial I_1} + \frac{\partial W_m}{\partial I_2}\right), \tag{8}$$

where $\partial W_m/\partial I_1$ is computed from Eq. (7) and $\partial W_m/\partial I_2 = 0$, as the selected strain energy function depends only on the invariant I_1.

3.2. Strain energy of nanofiller

The experimental tests in Section 2 revealed that adding GNPs increases the initial stiffness of the PNCs but diminishes the strain-stiffening response at large strains, primarily due to the gradual detachment of nanoparticles from the matrix as strain increases. With higher GNP content, the filler detachment and thus the reduction in strain

stiffening becomes more pronounced. This implies that if we define the residual stress as the difference between the stress of the PNC and that of the elastomer matrix, the residual stress exhibits a softening behavior. Therefore, the SE function of the nanofiller contribution must capture two key behaviors: the increase in initial stiffness and the softening effect due to detachment, which becomes more pronounced with increasing GNP content.

A phenomenological approach to hyperelastic softening was proposed by Volokh (2007, 2010), primarily aimed at modeling material failure. The core idea is that the energy increment, as the deformation process advances, should be limited to a critical value. This means that as $\|\mathbf{C}\| \to \infty$, the strain energy W_n approaches a constant value ϕ, often referred to as material failure energy. Following this approach, Volokh proposed an exponential form of softening hyperelasticity, which has been successfully applied to simulate material failure.

In the present work, we extend the softening hyperelasticity to a more general form that reproduces the contribution of nanofillers observed from our experiments. As our focus is on a broader softening response induced by the incorporation of nanofillers, rather than exclusively on material failure, we refer to ϕ as the limiting energy. We propose a SE function for the contribution of nanofiller given by

$$W_n = \psi_n \left[1 + \left(\frac{\psi_n}{\phi}\right)^{\beta}\right]^{-1/\beta}, \quad \text{with} \quad \psi_n = \frac{N}{3^{\alpha}}\left(I_1^{\alpha} - 3^{\alpha}\right), \tag{9}$$

where N is a material parameter related to elastic stiffness, and $\alpha \geq 1$ and $\beta > 0$ are dimensionless fitting parameters. Term $\psi_n(\mathbf{F})$ in Eq. (9) represents the energy of the intact material without softening, while the total energy of the nanofiller contribution, $W_n = W_n(\psi_n(\mathbf{F}))$, includes softening. In fact, as $\|\mathbf{F}\| \to \infty$, ψ_n approaches infinity, while W_n converges to ϕ. Conversely, if the limiting energy ϕ goes to infinity, W_n tends to ψ_n, indicating no softening. Note that in the expression for ψ_n, the parameter N is divided by 3^{α} to account for the fact that the actual strain measure is $I_1/3$, as discussed earlier in this section.

The form of ψ_n in Eq. (9) corresponds to the one-term model, which is the I_1-based hyperelastic model proposed by Lopez-Pamies (2010) with $M = 1$. The model involves two fitting parameters, N and α. We chose this SE function for the following reasons: (i) it offers mathematical simplicity and effectiveness for a wide range of deformations; (ii) it involves only I_1, a scalar strain measure that captures the variations in the length of line elements averaged over all orientations. This is ideal for representing the contributions of randomly oriented nanofillers in the elastomer, where deformation predominantly results from the stretching of molecular chains; (iii) in Lopez-Pamies (2010) the author demonstrated that the material parameters have physical significance, which aids in guiding the fitting process.

Softening in W_n is governed by the term in Eq. (9) that multiplies ψ_n, with parameters ϕ and β. The advantage of this proposed softening function lies in its versatility in reproducing different rates of softening. A lower value of β results in a slower softening process, while higher values lead to more rapid softening. This is illustrated in Fig. 7(a), which shows that increasing β results in a sharper decline in the strain energy.

The first Piola–Kirchhoff stress tensor associated with the nanofiller contribution, derived from Eq. (6) using the chain rule, is given by

$$\mathbf{P}_n = -p_n\mathbf{F}^{-T} + \frac{\partial \psi_n}{\partial \mathbf{F}}\left[1 + \left(\frac{\psi_n}{\phi}\right)^{\beta}\right]^{-(1+\beta)/\beta}, \quad \text{with} \quad \frac{\partial \psi_n}{\partial \mathbf{F}} = 2\mathbf{F}\frac{\partial \psi_n}{\partial I_1}. \tag{10}$$

The term multiplying $\partial\psi_n/\partial\mathbf{F}$ tends to zero as ψ_n approaches infinity, resulting in strain softening. In the case of uniaxial loading, the stress–stretch relation is

$$\sigma_{x,n} = 2\left(\lambda_x - \frac{1}{\lambda_x^2}\right)\frac{\partial \psi_n}{\partial I_1}\left[1 + \left(\frac{\psi_n}{\phi}\right)^{\beta}\right]^{-(1+\beta)/\beta}, \tag{11}$$

with $\partial\psi_n/\partial I_1 = 3^{-\alpha} N\alpha\, I_1^{\alpha-1}$ and $I_1 = 2/\lambda_x + \lambda_x^2$. The effect of parameter β on the stress associated to the nanofiller contribution, $\sigma_{x,n}$, is depicted in Fig. 7(b). Lower values of β produce a smooth and slow decrease in the tangent stiffness, while higher values result in sharper and more abrupt softening. The effect of varying the limiting energy ϕ is shown in Fig. 7(c).

In Appendix B, Eq. (B.1), we present the expression of the fourth-order tangent moduli tensor, a quantity of particular importance in computational mechanics, especially in FE methods (Itskov, 2000). We also derive the expression for the elastic modulus of the nanofiller contribution, $E_n = 2\alpha N$. As expected, the term introduced for the softening in the strain energy, Eq. (9), does not affect the elastic quantities in the linear elasticity regime.

4. Fitting of model parameters to uniaxial response

In this section, we calibrate the model parameters to reproduce the experimental data from uniaxial tests conducted on PNCs. The uniaxial stress–stretch relation for the nanocomposite is

$$\sigma_x = (1 - f)\sigma_{x,m} + f\sigma_{x,n}, \tag{12}$$

where $\sigma_{x,m}$ and $\sigma_{x,n}$ are given respectively by Eqs. (8) and (11). The additive decomposition allows us to independently calibrate the model parameters of the elastomer matrix (A, B, C_{10}, and I_m) by fitting $\sigma_{x,m}$ to experimental data of the silicone alone. Subsequently, we compute the residual stress as

$$\sigma_{x,\text{res}} = \sigma_{x,\text{exp}} - (1 - f)\sigma_{x,m}, \tag{13}$$

where $\sigma_{x,\text{exp}}$ represents the experimental data obtained from simple tension tests on PNCs. For each GNP content tested, a set of residual stress data is computed. The contribution of the nanofiller, $f\sigma_{x,n}$, is then fitted to the residual stress data $\sigma_{x,\text{res}}$, allowing us to obtain the model parameters N, ϕ, α, and β involved in the SE function W_n.

As observed from the experiments in simple tension (Section 2.2), the influence of GNPs varies with their content inside the nanocomposite. Increasing the content of GNPs leads to an increase in elastic stiffness, but it also affects the response in large stretches by reducing strain stiffening. The rule of mixtures, which linearly weighs the contributions W_m and W_n of the matrix and nanofiller, is not sufficient to fully capture the changing behavior. As GNP content varies, the parameters inside W_n change to accurately describe the qualitatively different responses of the PNCs. Therefore, in general, we have that $N = N(f)$, $\phi = \phi(f)$, $\alpha = \alpha(f)$, and $\beta = \beta(f)$.

Parameters α and β are mathematical exponents in the functions involved and primarily influence the nonlinear response and the softening at moderate to large strains, respectively. In contrast, N and ϕ have clearer physical meanings, as they respectively represent the contributions of nanofiller to initial stiffness and the limit energy for softening. For these reasons, in a specific PNC, it is expected that the qualitative changes with variations in GNP content are already well captured by variations in N and ϕ, allowing α and β to remain fixed. This ensures the physical soundness and simplicity of the model, thereby enhancing its predictive capability. Consequently, the model involves exponents α and β that do not vary with GNP content, while the variations in parameters N and ϕ are taken into account by estimating fitting laws $N(f)$ and $\phi(f)$ as functions of GNP content. A scheme of the framework for the fitting procedure and estimation of laws defining the model parameters is given in Fig. 8.

For convenience in the fitting process, we define the following nondimensional fitting parameters:

$$\bar{N} = 2f\alpha\frac{N}{E_m}, \quad \bar{\phi} = f\frac{\phi}{W_{m,u}}, \tag{14}$$

where $W_{m,u}$ is the ultimate value of W_m, corresponding to the deformation at which the elastomer matrix reached failure. In this way, the expression of the Young's modulus of the nanocomposite becomes:

$$E_c = E_m\left[(1 - f) + \bar{N}\right], \tag{15}$$

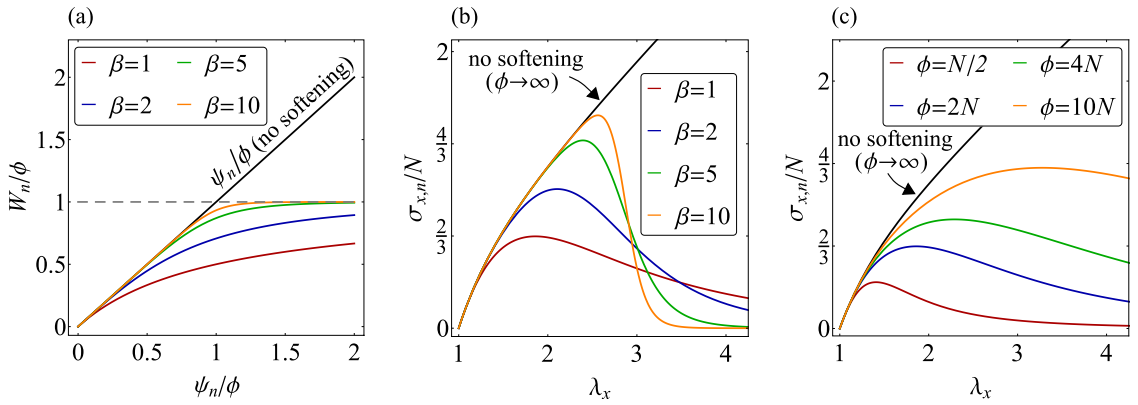

Fig. 7. Softening in the hyperelastic model for the nanofiller contribution. (a) Plot of normalized strain energy with softening W_n/ϕ vs. normalized strain energy of intact material ψ_n/ϕ, showing the effect of variations in β. (b) Plot of normalized uniaxial stress $\sigma_{x,n}/N$ vs. stretch λ_x, illustrating that β regulates the sharpness of the softening, with $\phi = 2N$ and $\alpha = 1$. (c) Plot of $\sigma_{x,n}/N$ vs. λ_x showing the effect of variations in the limiting energy ϕ, with β and α fixed at 1.

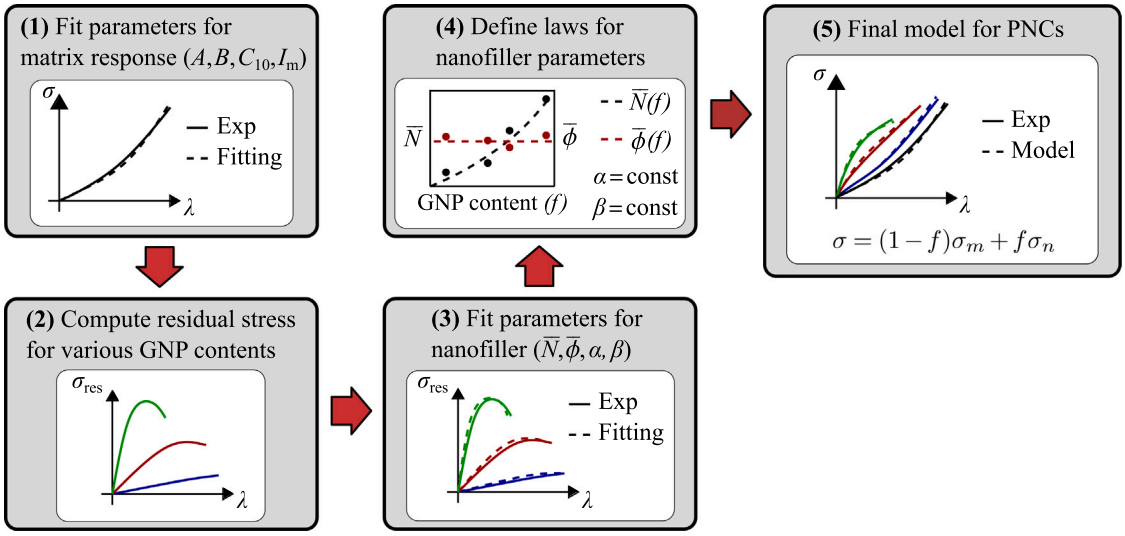

Fig. 8. Schematic representation of the steps for calibrating the hyperelastic model of PNCs.

which indicates that $\bar{N}$ represents the increment in Young's modulus due to the nanofiller contribution, normalized with respect to E_m. Similarly, $\bar{\phi}$ represents a normalization of the limiting energy with respect to the ultimate value of strain energy of the matrix. These definitions allow for easier handling of the parameter ranges during the fitting process.

The material parameters of the silicone matrix were determined by fitting the stress $\sigma_{x,m}$ predicted by the model, as expressed in Eq. (8), to the experimental σ_x vs. λ_x data of silicone reported in Fig. 4(a). This fitting was conducted using the *FindFit* function in *Wolfram Mathematica*. The fitting parameters are reported in Table C.1 of Appendix C, and the corresponding stress–stretch curve is displayed in Fig. 9(a). Subsequently, the residual stress data $\sigma_{x,\text{res}}$ vs. λ_x for each GNP content were computed using Eq. (13). The contribution of the nanofiller, given by $f\sigma_{x,n}$ where $\sigma_{x,n}$ is expressed by Eq. (11), was then fitted to the residual stress data using *FindFit* in *Wolfram Mathematica*. This fitting process was initially conducted without any specific restrictions on parameter ranges to observe if certain parameters tended to show a consistent trend or assumed values close to constants. It was observed that parameters α and β consistently tended to have values around 2 and 1, respectively. Consequently, their values were fixed to $\alpha = 2$ and $\beta = 1$. The fitting was then performed again, considering only the unknown parameters $\bar{N}$ and $\bar{\phi}$, resulting in optimal values reported in Table C.1. The plots of residual stress curves obtained from the fitting are shown in Fig. 9(b).

The final uniaxial response of the PNCs was computed by summing the contributions of the matrix and nanofiller, as described in Eq. (12). The plot in Fig. 9(c) displays the model curves alongside the experimental data. The model demonstrates a good capability to describe the behavior, including both stiffness increase and influence on strain stiffening in large deformations. With parameters α and β fixed, the model provides a good description of the softening observed in the residual stress (Fig. 9(b)), while maintaining simplicity and a physical basis.

The final step of the fitting process involved estimating laws to describe $\bar{N}(f)$ and $\bar{\phi}(f)$ as functions of GNP content. The optimal values of both parameters, obtained from the previous fitting and listed in Table C.1, are plotted in Fig. 10(a). As shown, the values of $\bar{N}$ increase with the GNP content. This aligns with its physical meaning, as $\bar{N}$ quantifies the contribution of nanofillers to the initial stiffness of the nanocomposite, which increases as the GNP content rises. To fit the data, we selected a power-law model and obtained the following fitting function:

$$\bar{N}(f) = 343.6 f^{1.28} \tag{16}$$

where f represents the volume fraction of GNPs in the nanocomposite. Concerning the distribution of the $\bar{\phi}$ data, we chose to fit using a constant value, $\bar{\phi}(f) = 0.49$. This decision was based on the observation that, after a GNP content of 1 phr, the fitted values consistently cluster around 0.49. Therefore, for the sake of simplicity, we fixed its

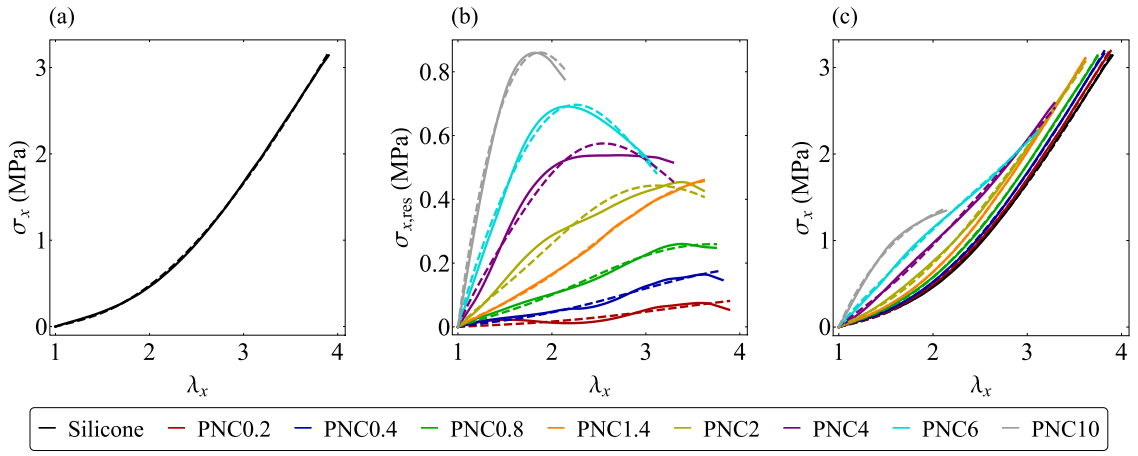

Fig. 9. Fitting of the model to experimental uniaxial data of PNCs. (a) Stress–stretch response obtained by fitting $\sigma_{x,m}$ to the data of the silicone matrix. (b) Fitting of the nanofiller contribution $f\sigma_{x,n}$ to the residual stress data for each of the analyzed GNP contents, with f representing the GNP volume fraction. (c) Final stress–stretch response of the model obtained by summing the contributions of the matrix and nanofiller, with model parameters reported in Table C.1. Dashed and solid lines represent the fitting model and the experimental data, respectively. The GNP contents reported in the legend are in phr.

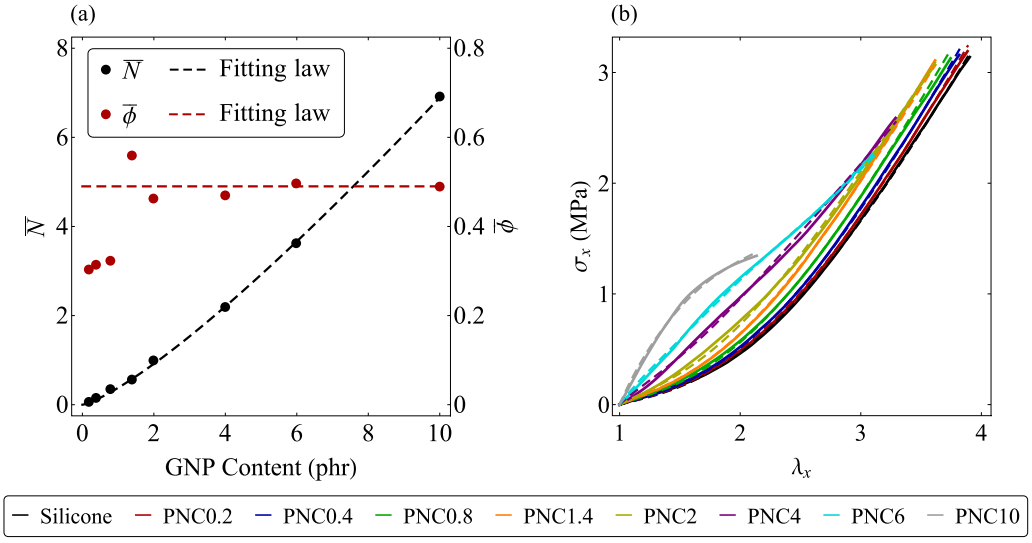

Fig. 10. Laws for the parameters involved in the nanofiller contribution and final model for the uniaxial response. (a) Values of parameters $\bar{N}$ and $\bar{\phi}$ with varying GNP content and their respective fitting laws, $\bar{N}(f)$ from Eq. (16) and $\bar{\phi} = 0.49$. (b) Final stress–stretch uniaxial response of PNCs modeled with $\alpha = 2$, $\beta = 1$, $\bar{N}(f)$ given in Eq. (16), and $\bar{\phi} = 0.49$. Dashed and solid lines represent the fitting model and the experimental data, respectively. The GNP contents reported in the legend are in phr.

value. Additionally, for low contents of GNPs, the softening behavior is much less pronounced than for higher contents, making the role of $\bar{\phi}$ secondary compared to $\bar{N}$.

The uniaxial response of PNCs with varying GNP contents, given by the final model with $\alpha = 2$, $\beta = 1$, $\bar{N}(f)$ given in Eq. (16), and $\bar{\phi} = 0.49$, provides the stress–stretch curves shown in Fig. 10(b). The quality of the prediction is slightly reduced compared to Fig. 9(c), but the model still accurately reproduces the uniaxial behavior of PNCs.

5. Fitting of model parameters to biaxial response

As it is well known, parameters calibrated from uniaxial tests do not generally provide accurate predictions for biaxial stress states. Therefore, in this section, we calibrate a set of model parameters to simulate the biaxial response of PNCs observed from inflation tests conducted on circular membranes.

The steps for calibrating the model follow those depicted in Fig. 8, but now in terms of pressure–deflection instead of stress–stretch relationships. Unlike simple tension tests, the inflation of circular membranes lacks an explicit analytical solution, making parameter fitting more complex. However, during our experiments on PNC membranes, their deformed shapes closely resembled a spherical cap. An approximate analytical solution under this assumption was derived in Pelliciari et al. (2022), expressing the pressure–deflection relation as

$$p = \frac{16\,\bar{\delta}^2 H \sin^5\varphi}{\left(\bar{\delta}^2+1\right)^2 \varphi^6 R}\left(\varphi^6 \csc^6\varphi - 1\right)\left(\frac{\partial W}{\partial I_1} + \frac{\partial W}{\partial I_2}\varphi^2 \csc^2\varphi\right), \tag{17}$$

where $\varphi = 2\tan^{-1}\bar{\delta}$. The accuracy of this approximate solution generally holds until the limit point instability is reached. Since our PNC membranes failed close to this point, the approximate formula is expected to provide an accurate description of their behavior. Therefore, this solution was used for initial parameter calibration. Subsequently, the final response to verify the calibration was obtained with an exact numerical solution, as will be detailed in the following.

The parameters of the elastomer matrix were calibrated based on the pressure–deflection response of pure silicone shown in Fig. 6. To achieve this, Eq. (17) was evaluated for the elastomer matrix ($W = W_m$), yielding the expression of p_m as a function of $\bar{\delta}$. Using *FindFit* in *Wolfram Mathematica*, we fitted p_m to the experimental curve and obtained the optimal values of A, B, C_{10}, and I_m listed in Table C.2.

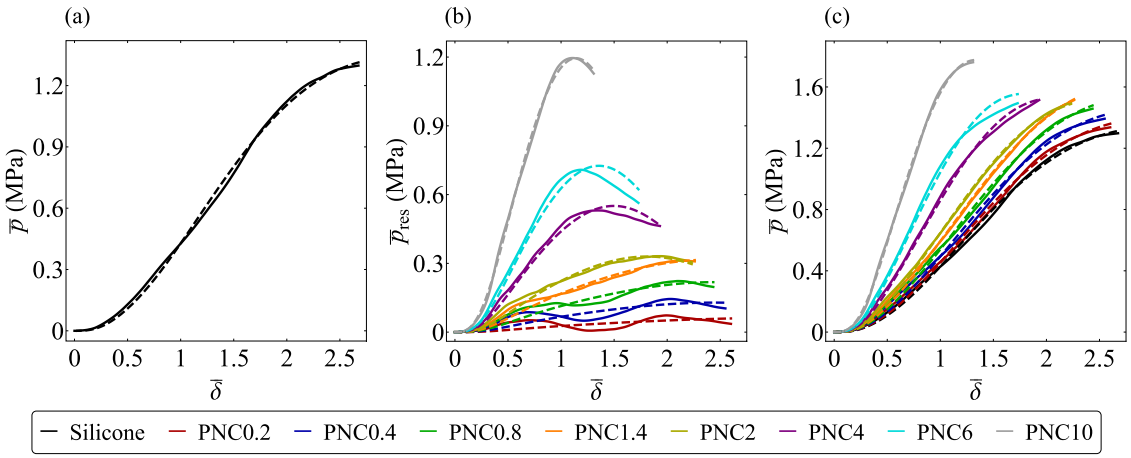

Fig. 11. Fitting of the model to experimental biaxial (inflation) data of circular PNC membranes. (a) Pressure–deflection response obtained by fitting the approximate analytical solution, p_m, to the data of the silicone matrix. (b) Fitting of the nanofiller contribution using the approximate solution, $f p_n$, to the residual pressure data for each of the analyzed GNP contents, with f representing the GNP volume fraction. (c) Final pressure–deflection response of the model obtained by summing the contributions of the matrix and nanofiller, with model parameters reported in Table C.2. This final response was derived using the exact numerical solution, outlined in Appendix D. Dashed and solid lines represent the fitting model and the experimental data, respectively. The GNP contents reported in the legend are in phr. The pressure and displacement are normalized as $\bar{p} = pR/H$ and $\bar{\delta} = \delta/R$.

Fig. 11(a) shows the corresponding plot of the pressure–deflection curve. Subsequently, the residual pressure data were computed as

$$p_{\text{res}} = p_{\text{exp}} - (1 - f)p_m, \tag{18}$$

where p_{exp} represents the experimental pressure data from inflation tests on PNCs. For each GNP content tested, a set of residual pressure data was computed. The contribution of the nanofiller, p_n, was obtained by evaluating Eq. (17) with $W = W_n$, and the expression $f p_n$ was fitted to the residual pressure p_{res}. The fitting curves are displayed in Fig. 11(b). The obtained values of parameters $\bar{N}$, $\bar{\phi}$, α, and β are reported in Table C.2. Note that α and β were fixed respectively to the values 1.75 and 1.25, while $\bar{N}$ and $\bar{\phi}$ varied with the GNP content.

After calibrating the fitting parameters with the approximate formula, we adopted the numerical solution reported in Appendix D, which is valid for incompressible membranes subjected to inflation. The SE function for PNCs, $W = (1 - f)W_m + fW_n$, with W_m and W_n given in Eqs. (7) and (9) respectively, was integrated into the equilibrium equations. These equations were implemented in MATLAB, and simulations were conducted for all GNP contents using the fitting parameters of Table C.2. The numerical pressure–deflection curves obtained are displayed in Fig. 11(c), alongside the experimental data from the inflation tests. We observe that the curves match well the experimental responses, confirming the effectiveness of using the approximate analytical solution, Eq. (17), for deriving the fitting parameters. Note that this effectiveness is attributed to the fact that the analyzed membranes deform similarly to a spherical cap during inflation and reach failure before the onset of limit point instability.

Finally, we estimated laws to describe $\bar{N}(f)$ and $\bar{\phi}(f)$ as functions of GNP content. The fitting values of both parameters, listed in Table C.2, are plotted in Fig. 12(a). We fitted the data of $\bar{N}$ with the following power-law model:

$$\bar{N}(f) = 0.782(10^2 f)^{0.806+6.59f}. \tag{19}$$

For simplicity, the values of $\bar{\phi}$ were fitted with the constant $\bar{\phi}(f) = 0.53$, although this fit is not particularly accurate for low GNP contents. However, for low GNP contents, the effect of $\bar{\phi}(f)$ is less pronounced because there is less softening to be simulated. Therefore, even a very approximate fit in this range still provides reasonable results, considering the advantage in simplicity and ease of interpretation.

The pressure–deflection response of circular PNC membranes with varying GNP contents, given by the final model with $\alpha = 1.75$, $\beta = 1.25$, $\bar{N}(f)$ given in Eq. (19), and $\bar{\phi} = 0.53$, was computed using the exact numerical solution in MATLAB. The pressure–deflection curves are shown in Fig. 12(b), indicating that the quality of the prediction is slightly reduced compared to Fig. 11(c). However, the model demonstrates that even with simple formulations, it is capable of providing a good description of the overall pressure–deflection curve of PNC membranes. If greater accuracy is required, one may consider refining the law for $\bar{\phi}(f)$.

We emphasize that the primary objective of the model calibration in this section was to accurately replicate the pressure–deflection behavior of circular PNC membranes, which holds practical relevance. However, for a thorough characterization of the biaxial behavior, additional experimental data may be necessary, and a more comprehensive SE function should be considered for the elastomer matrix. While the I_1-based function employed here suffices for our targeted analyses, it does not generally provide a comprehensive description of biaxial behavior. In fact, previous studies have underscored the importance of including I_2 to capture biaxial responses and shear deformations (Anssari-Benam et al., 2021; Kuhl and Goriely, 2024). Therefore, for a more detailed examination of biaxial or other complex stress states, adopting a form of W_m in Eq. (9) that includes both I_1 and I_2 is advisable. For instance, hyperelastic functions for elastomers that are based on both invariants and employed in nonlinear elasticity are reported in Dal et al. (2021), Venkata et al. (2024), Destrade et al. (2017).

6. Application to other experimental data

In this section, we apply the proposed hyperelastic model for PNCs to experimental data from uniaxial tests found in the literature. The goal is to demonstrate that the model can be effectively applied to large deformations of PNCs beyond the specific cases studied in this work. The following experimental datasets were considered:

- *Dataset 1*: Reported by Frogley et al. (2003), this study involved uniaxial tensile tests on nanocomposites comprising single-wall CNTs mixed into an RTV silicone rubber matrix.
- *Dataset 2*: Presented by Young et al. (2018), this research focused on uniaxial tensile tests on nanocomposites that integrate GNPs into a thermoplastic elastomer (TPE), specifically Alcryn 2265.
- *Dataset 3*: Described by Xing et al. (2014), this dataset includes results from uniaxial tensile tests on nanocomposites made by incorporating graphene nanosheets (GE) into a natural rubber (NR) matrix.

The data were digitized, and Fig. 13 presents the stress–stretch curves of the three datasets considered.

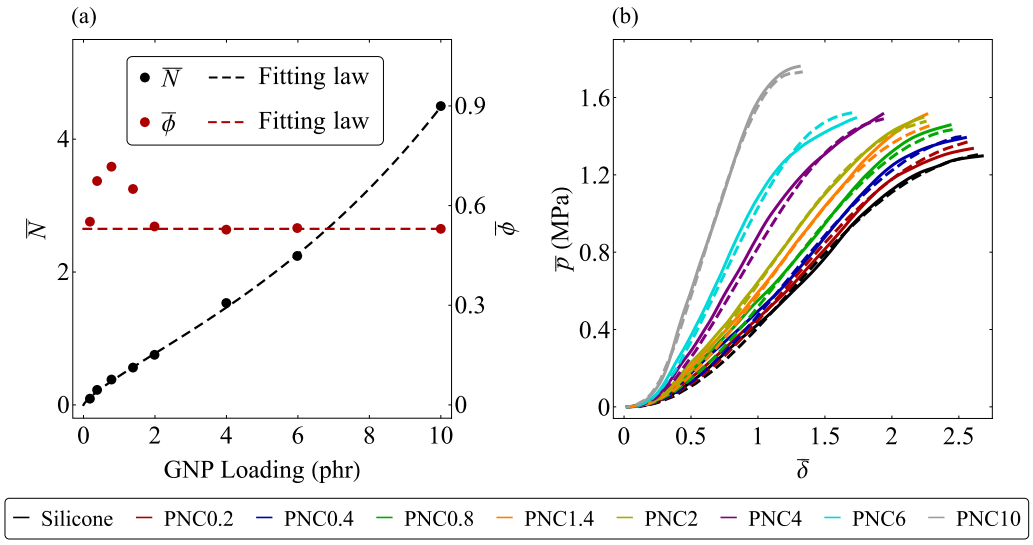

Fig. 12. Laws for the parameters involved in the nanofiller contribution and final model for the biaxial (inflation) response of circular PNC membranes. (a) Values of parameters $\bar{N}$ and $\bar{\phi}$ with varying GNP content and their respective fitting laws, $\bar{N}(f)$ from Eq. (19) and $\bar{\phi} = 0.53$. (b) Final pressure–deflection response of PNCs modeled by the numerical solution for circular inflated membranes (Appendix D), with $\alpha = 1.75$, $\beta = 1.25$, $\bar{N}(f)$ given in Eq. (19), and $\bar{\phi} = 0.53$. Dashed and solid lines represent the numerical solution and the experimental data, respectively. The GNP contents reported in the legend are in phr.

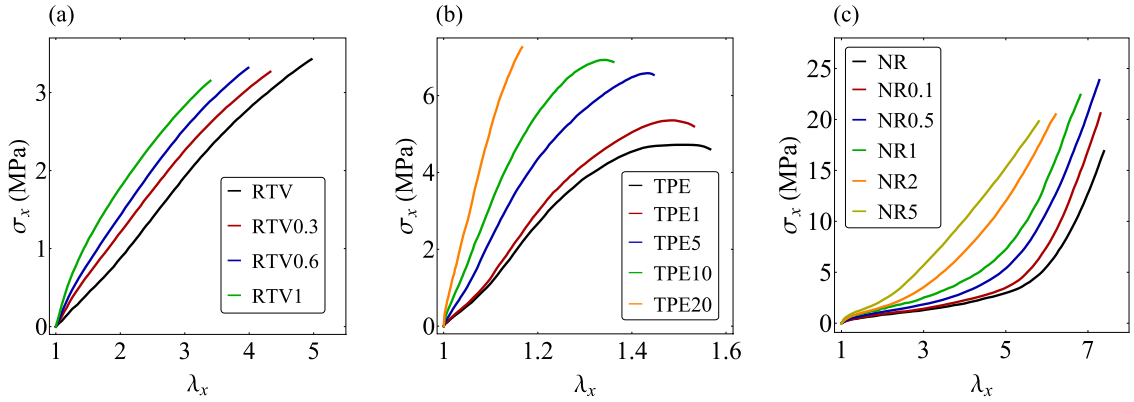

Fig. 13. Experimental stress–stretch data from uniaxial tests reported in the literature. (a) *Dataset 1* by Frogley et al. (2003), featuring RTV silicone rubber mixed with single-wall CNTs. (b) *Dataset 2* by Young et al. (2018), involving TPE mixed with GNPs. (c) *Dataset 3* by Xing et al. (2014), showing NR mixed with GE. For each dataset, the legend indicates the nanofiller content expressed in phr.

The datasets relate to PNCs composed of various elastomers, each exhibiting distinct behaviors that are generally not well-predicted by a single strain energy function W_m for the matrix contribution. Therefore, for each dataset, we selected a specific form of W_m that accurately fits the observed stress–stretch response of the sole matrix. This SE of the matrix was then introduced in the total strain energy of the PNC, $W = (1 - f)W_m + fW_n$, with the nanofiller contribution W_n defined by the proposed function in Eq. (9).

In the following, we describe the SE functions selected for the elastomeric matrices of each dataset considered:

- The stress–stretch curve of the RTV silicone from *Dataset 1*, as shown by Fig. 13(a), exhibits slight strain stiffening at moderate stretches. However, as the stretch increases, some softening is observed before the material reaches failure. To accurately replicate this material response, we employed the Mooney–Rivlin model with softening as proposed by Volokh (2007) for modeling material failure. The function is expressed as

$$W_m = \phi_v - \phi_v e^{-[C_{10}(I_1-3)+C_{01}(I_2-3)]/\phi_v}, \tag{20}$$

  where C_{10} and C_{01} are the material parameters of the Mooney–Rivlin model, and ϕ_v represents the material failure energy, as defined by Volokh.

- For *Dataset 2*, the stress–stretch curve of the TPE (Fig. 13(b)) exhibits a pattern similar to that of the RTV silicone, with strain stiffening followed by more pronounced softening prior to failure. Given the similar behavior, we adopted the same function for W_m as in Eq. (20).
- The NR matrix from *Dataset 3*, as displayed in Fig. 13(c), exhibits the typical uniaxial tensile response of elastomers. Specifically, at large stretches, strain stiffening becomes predominant until the material reaches failure. This classic response can be effectively modeled using several hyperelastic models designed for such behaviors. For this analysis, we employ the Carroll model (Carroll, 2011), which is characterized by the following strain energy function:

$$W_m = AI_1 + BI_1^4 + CI_2^{1/2}, \tag{21}$$

  where A, B, and C are material fitting parameters.

For each of the three datasets considered, we calibrated the model parameters following the procedure outlined in Fig. 8, which was previously implemented in Section 4. Initially, we obtained the fitting parameters for the selected SE functions for W_m, which are listed in Table C.3. Subsequently, we computed the residuals for each of the nanofiller contents and estimated the optimal parameters $\bar{N}$, $\bar{\phi}$, α, and

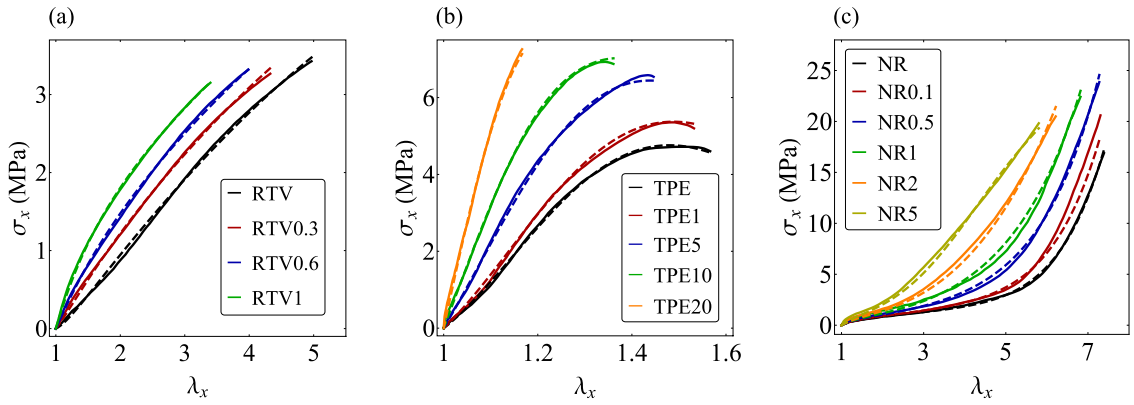

Fig. 14. Application of the proposed model to experimental uniaxial stress–stretch data from the literature. (a) *Dataset 1* by Frogley et al. (2003), (b) *Dataset 2* by Young et al. (2018), and (c) *Dataset 3* by Xing et al. (2014). Model parameters for the matrix are reported in Table C.3, and for the nanofiller contributions in Eqs. (22)–(24). Dashed and solid lines represent the model fitting and the experimental data, respectively. Legends indicate the nanofiller content expressed in phr.

β for the nanofiller contribution W_n. Finally, we derived fitting laws to predict the model parameters as functions of the nanofiller content, expressed as the volumetric fraction f. The resulting functions and parameters of W_n for the three datasets are as follows:

- *Dataset 1*

$$\alpha = 1, \quad \beta = 0.6, \quad \bar{N}(f) = 658.1f, \quad \bar{\phi}(f) = 0.344 + 146.5f \tag{22}$$

- *Dataset 2*

$$\alpha = 2, \quad \beta = 1.2, \quad \bar{N}(f) = 55.9f, \quad \bar{\phi}(f) = 4.1f^{0.443} \tag{23}$$

- *Dataset 3*

$$\alpha = 2.1, \quad \beta = 1, \quad \bar{N}(f) = 17.61f^{0.853+0.5f}, \quad \bar{\phi}(f) = 13.14\,e^{-63.6f} \tag{24}$$

The corresponding stress–stretch curves, presented alongside the experimental data, are shown in Fig. 14.

The model provides sufficiently accurate fitting of the experimental data considered. Particularly, the stress–stretch response from *Dataset 1* is relatively simple, primarily characterized by an increase in initial stiffness and only a slight influence on strain stiffening with an increase in CNT content. In fact, linear functions for $\bar{N}(f)$ and $\bar{\phi}(f)$ provide satisfactory results. The behaviors from *Dataset 2* and *Dataset 3* exhibit more complex trends, which are observed partly because the GNP and GE contents are higher than those in *Dataset 1*. Thus, more complex fitting functions for $\bar{N}(f)$ and $\bar{\phi}(f)$ were required to achieve good accuracy.

7. Conclusions

We investigated the mechanical behavior of PNCs composed of silicone and GNPs through simple tension and inflation tests. Consistent with other experimental studies, we found that the introduction of nanofillers not only significantly increases the initial stiffness in the small strain regime but also affects the nonlinear behavior at large strains. Particularly, increasing nanofiller content reduces sensibly the strain stiffening of the elastomer and its failure strain.

We developed a strain energy function that incorporates two separate contributions: W_m, representing the elastomer matrix, and W_n, representing the nanofiller. Accordingly, W_m was independently calibrated using experimental data solely from the elastomer, while W_n was calibrated by fitting the residual stresses derived from tests on the PNCs. For the nanofiller contribution, we proposed a novel function tailored to replicate the experimentally observed behavior, and to predict the response as a function of the nanofiller content.

The proposed model proved capable of accurately reproducing the mechanical response of PNCs under both uniaxial and biaxial (inflation) stress states. For simple tension, an established analytical solution was used, while for the inflation of circular membranes, we implemented the new strain energy function in a MATLAB numerical code to obtain the exact numerical solution. Additionally, we applied the model to replicate the behavior of other PNCs using experimental data available in the literature, demonstrating its broader applicability.

This hyperelastic model represents an important advancement over previous studies, which generally did not address the specific effects of graphene nanofillers under large deformations, often lacked comparisons with experimental data, and focused predominantly on uniaxial data. In contrast, we aimed to develop a model that captures the nonlinear effects of nanoparticles under large strains, with experimental observations serving to support the development and validation of our model. Given the significance of the topic in both research and engineering technologies, the proposed model offers a robust foundation for employing PNCs effectively.

Future research will focus on a more in-depth analysis of the interactions between nanoparticles and the elastomer matrix, with the goal of developing a comprehensive multiscale modeling approach. In our current model, interfacial debonding of nanoparticles from the matrix was incorporated on a phenomenological basis, as observations showed that debonding affected the macroscale mechanical response by introducing softening. Future detailed analyses using advanced electron microscopy may enable a more thorough examination of this effect and help establish connections between microscale phenomena and the macroscopic continuum model. Additionally, by closely examining the formation of aggregates, we aim to incorporate more precise descriptions of this process into the model. Finally, we are conducting ongoing research to extend the hyperelastic model to PNCs reinforced with carbon nanotubes.

CRediT authorship contribution statement

Matteo Pelliciari: Writing – review & editing, Writing – original draft, Resources, Project administration, Methodology, Investigation, Formal analysis, Conceptualization, Supervision. **Stefano Sirotti:** Writing – review & editing, Software, Investigation, Data curation. **Angelo Aloisio:** Resources, Data curation. **Angelo Marcello Tarantino:** Funding acquisition.

Declaration of competing interest

The authors declare that they have no known competing financial interests or personal relationships that could have appeared to influence the work reported in this paper.

Acknowledgments

This work was supported by the Italian Ministry of University and Research (MUR) through research grants PRIN 2020 No. 2020EBLPLS on "Opportunities and challenges of nanotechnology in advanced and green construction materials", and PRIN 2022 PNRR No. P2022AHFCP on "New challenges of thin-walled structures at large strains and their promising applications". Additional financial support was provided by the University of Modena and Reggio Emilia for the project "FAR Dipartimentale 2024-2025" (CUP E93C24000500005). Support by the National Group of Mathematical Physics (GNFM-INdAM) is also acknowledged. The authors extend their gratitude to Eng. Pasqualino Gualtieri for his valuable assistance in the experiments on PNC membranes and to Eng. Giacomo Gramantieri for kindly 3D printing dog-bone-shaped and circular molds.

Appendix A. Microscopy and DIC analyses

This appendix presents microscopy images of the produced PNC samples and a detailed description of the DIC analysis used to determine pole stretch during inflation tests on circular membranes.

A.1. Microscopy images

Optical microscopy images were obtained to examine the dispersion, morphology, and size of GNPs within the produced PNC samples. The samples were cut to expose the internal structure and then observed under optical microscopy. The resulting images are shown in Fig. A.15.

Fig. A.15(a) shows the pure silicone matrix, while Figs. A.15(b)–(d) illustrate the increasing presence of GNPs (dark regions) as the content rises to 0.8, 2, and 6 phr, respectively. Two important observations can be made from these images. First, the nanoparticles are well-dispersed within the matrix, exhibiting a random orientation, which indicates that the mixing process during production was effective. Second, at a GNP content of 0.8 phr, only minimal aggregation appears, with few larger dark regions visible. As expected, with higher filler content, the nanoparticles increasingly interact and form aggregates, especially noticeable in Fig. A.15(d). However, at these relatively high GNP concentrations, such aggregation behavior is typical and generally unavoidable (Chieng et al., 2013; Zare, 2016b). Therefore, the nanoparticle distribution remains satisfactory, even at higher filler levels.

Finally, Figs. A.15(e) and (f) present higher magnification images of the PNC sample with 0.8 phr GNP content, clearly illustrating the morphology of the GNPs within the matrix. When nanoplatelets are in close proximity, they naturally tend to interact, forming aggregations, visible in detail in the high-magnification image in Fig. A.15(f). This aggregation trend is typical and, as previously noted, expected as the GNP content increases.

A.2. DIC analysis for membrane pole stretch

In the following, we outline the DIC analysis conducted using *Ncorr* to determine the pole stretch of the membranes during inflation tests. To ensure image correlation by the software, the membranes were prepared with superficial patterns. Silicone membranes were marked with a black pattern, while PNC membranes were marked with a red pattern. Initially, PNC membranes were black, suggesting that a white pattern would be optimal. However, significant deformations during inflation caused the silicone matrix to crystallize, resulting in the PNC membranes appearing white. Consequently, we opted for red paint to create the pattern, ensuring consistent contrast throughout the test.

We extracted 300 frames from the video of each test and loaded all frames into *Ncorr*. Figs. A.16(a) and (b) show four distinct frames during the inflation of the silicone membrane and PNC membrane with 2 phr GNP content, respectively.

We defined the ROI for both silicone and PNC membranes with a circular shape around the pole, as depicted in Figs. A.16(c) and (d). We performed a high-strain analysis, which provided the values of ε_x and ε_y during the inflation tests. As expected, the contour plots of the strain components along both the x and y directions reveal a central area within the ROI where the strain is higher. Additionally, the maximum values of ε_x and ε_y within this area are nearly identical. This is because during the inflation of circular membranes, the pole represents the only point where the stress and strain states are equibiaxial, while all other points exhibit non-equibiaxial states. We computed the average of these maximum values, referring to it as ε_{max}. The pole stretch was then computed as $\lambda = \sqrt{1+2\varepsilon_{max}}$ and synchronized with the pressure data to extract the pressure vs. pole stretch curves depicted in Fig. 6(b).

We remark that the inflation of circular membranes exhibits axial symmetry, meaning that strain data can be reliably obtained only at the pole when using a single camera. In fact, we concentrated our analysis on a specific ROI centered around the pole and extracted only the maximum strain. Achieving a three-dimensional reconstruction of the strain field would require more sophisticated techniques, such as employing multiple cameras and advanced DIC technology. Though simple, our approach proved effective in capturing the pole stretch, our primary focus.

Appendix B. Tangent moduli tensor

The fourth-order tangent moduli tensor is expressed by

$$\mathcal{L}_n = \frac{\partial^2 W_n}{\partial \mathbf{F}^2} = 4\left[\frac{\partial^2 W_n}{\partial \psi_n^2}\left(\frac{\partial \psi_n}{\partial I_1}\right)^2 + \frac{\partial W_n}{\partial \psi_n}\frac{\partial^2 \psi_n}{\partial I_1^2}\right]\mathbf{F}\otimes\mathbf{F} + 2\frac{\partial W_n}{\partial \psi_n}\frac{\partial \psi_n}{\partial I_1}\mathcal{I} \quad \text{(B.1)}$$

where $\otimes$ indicates the tensor product, $\mathcal{I}$ represents the fourth-order identity tensor, and

$$\begin{aligned}
\frac{\partial \psi_n}{\partial I_1} &= \frac{N}{3^\alpha}\alpha\, I_1^{\alpha-1},\\
\frac{\partial W_n}{\partial \psi_n} &= \left[1+\left(\frac{\psi_n}{\phi}\right)^\beta\right]^{-(1+\beta)/\beta},\\
\frac{\partial^2 \psi_n}{\partial I_1^2} &= \frac{N}{3^\alpha}\alpha(\alpha-1)\, I_1^{\alpha-2},\\
\frac{\partial^2 W_n}{\partial \psi_n^2} &= -\frac{\beta+1}{\psi_n}\left(\frac{\psi_n}{\phi}\right)^\beta\left[1+\left(\frac{\psi_n}{\phi}\right)^\beta\right]^{-(1+2\beta)/\beta}.
\end{aligned} \quad \text{(B.2)}$$

The above tensor vanishes with $\psi_n \to \infty$, indicating as expected that the tangent stiffness of the softened material response tends to zero when $\|\mathbf{F}\| \to \infty$. The case of the intact material is retrieved by taking the limit

$$\lim_{\phi\to\infty}\mathcal{L}_n = 4\frac{\partial^2 \psi_n}{\partial I_1^2}\mathbf{F}\otimes\mathbf{F} + 2\frac{\partial \psi_n}{\partial I_1}\mathcal{I}, \quad \text{(B.3)}$$

which corresponds with the expression reported in Lopez-Pamies (2010).

To derive the elastic modulus of the nanofiller contribution, we compute the tangent stiffness in the uniaxial response from Eq. (11) as

$$\begin{aligned}
\frac{\partial \sigma_{x,n}}{\partial \lambda_x} = {} & \frac{4}{\lambda_x^4}\left(\lambda_x^3-1\right)^2\left[\frac{\partial^2 W_n}{\partial \psi_n^2}\left(\frac{\partial \psi_n}{\partial I_1}\right)^2 + \frac{\partial W_n}{\partial \psi_n}\frac{\partial^2 \psi_n}{\partial I_1^2}\right]\\
& + \frac{2}{\lambda_x^3}\left(\lambda_x^3+2\right)\frac{\partial W_n}{\partial \psi_n}\frac{\partial \psi_n}{\partial I_1}.
\end{aligned} \quad \text{(B.4)}$$

Evaluating Eq. (B.4) in the undeformed configuration, $\lambda_x = 1$, gives the expression for the elastic modulus of the nanofiller contribution:

$$E_n = \left.\frac{\partial \sigma_{x,n}}{\partial \lambda_x}\right|_{\lambda_x=1} = 2\alpha N. \quad \text{(B.5)}$$

The elastic modulus of the polymer nanocomposite, described by the total strain energy given in Eq. (2), is thus expressed as

$$E_c = 6(1-f)\left(A + C_{10}\right) + 2f\alpha N. \quad \text{(B.6)}$$

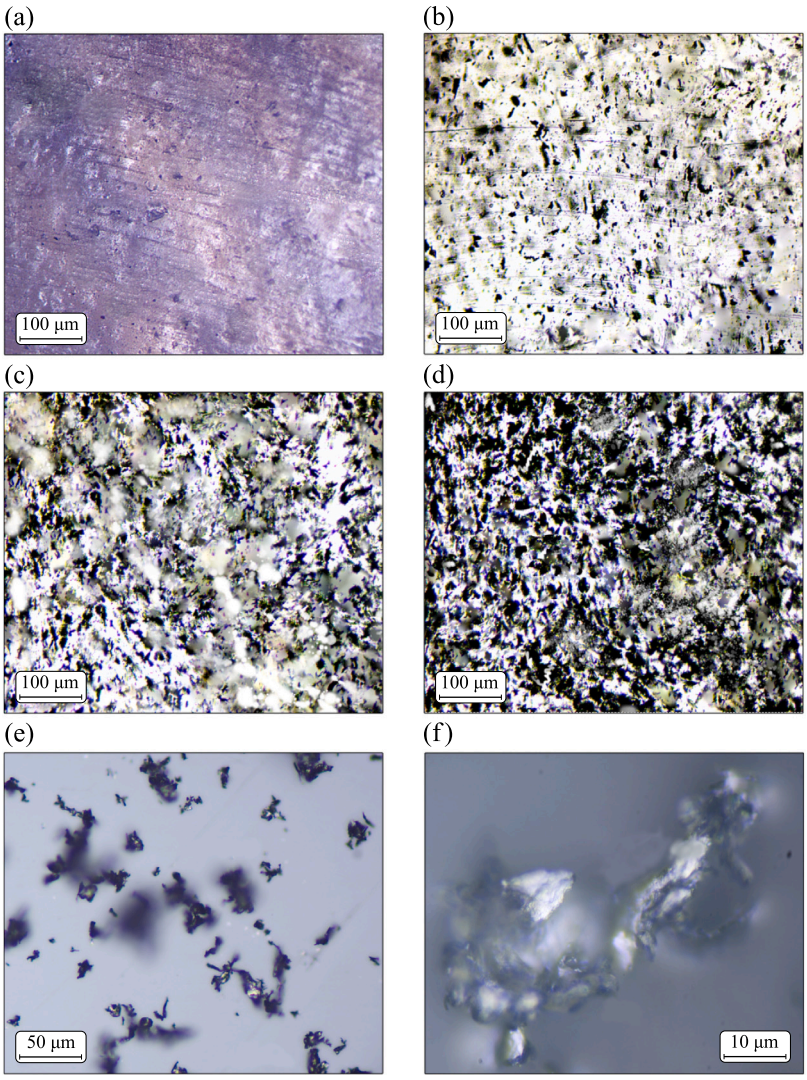

Fig. A.15. Optical microscopy images at a magnification of 100x for (a) pure silicone and PNCs with GNP contents of (b) 0.8 phr, (c) 2 phr, and (d) 6 phr. Higher magnification images of the sample with 0.8 phr content at (e) 200x and (f) 1000x provide a more detailed view of the nanofiller morphology.

Appendix C. Fitting parameters

The fitting parameters are presented below for the cases of uniaxial response in simple tension, biaxial response under inflation of circular membranes, and the application of the model to additional experimental data from the literature.

C.1. Simple tension

Table C.1 presents the parameters obtained from fitting to uniaxial tensile data, as described in Section 4. Note that parameters $\bar{N}$ and $\bar{\phi}$, as defined in Eq. (14), require the estimation of the elastic modulus E_m and the ultimate value of the strain energy $W_{m,u}$ of the matrix. For the silicone considered in this work, E_m was estimated to be 0.326 MPa, as reported in Fig. 5, and $W_{m,u}$ was computed as 3.364 MPa by evaluating the strain energy from Eq. (7) at the ultimate stretch of the silicone in the uniaxial tensile test.

Table C.1
Values of parameters for matrix and nanofiller contributions, W_m and W_n, resulting from fitting to uniaxial experimental data. Units are in MPa where applicable.

Matrix parameters	Nanofiller parameters				
	GNP content (phr)	α	β	$\bar{N}$	$\bar{\phi}$
A = −0.515	0.2	2	1	0.0543	0.302
	0.4	2	1	0.151	0.314
B = 0.0886	0.8	2	1	0.349	0.322
	1.4	2	1	0.558	0.558
C_{10} = 0.565	2	2	1	0.988	0.462
	4	2	1	2.19	0.469
I_m = 499	6	2	1	3.61	0.496
	10	2	1	6.91	0.489

We provide here a note on the values of the parameter $\bar{N}$ obtained from the fitting process. This parameter represents the relative contribution of GNPs to the composite's elastic modulus compared to the matrix alone. Two considerations are as follows:

(1) Despite the low volume content, the nanofillers contribute significantly to the initial stiffness of the composite. The relative

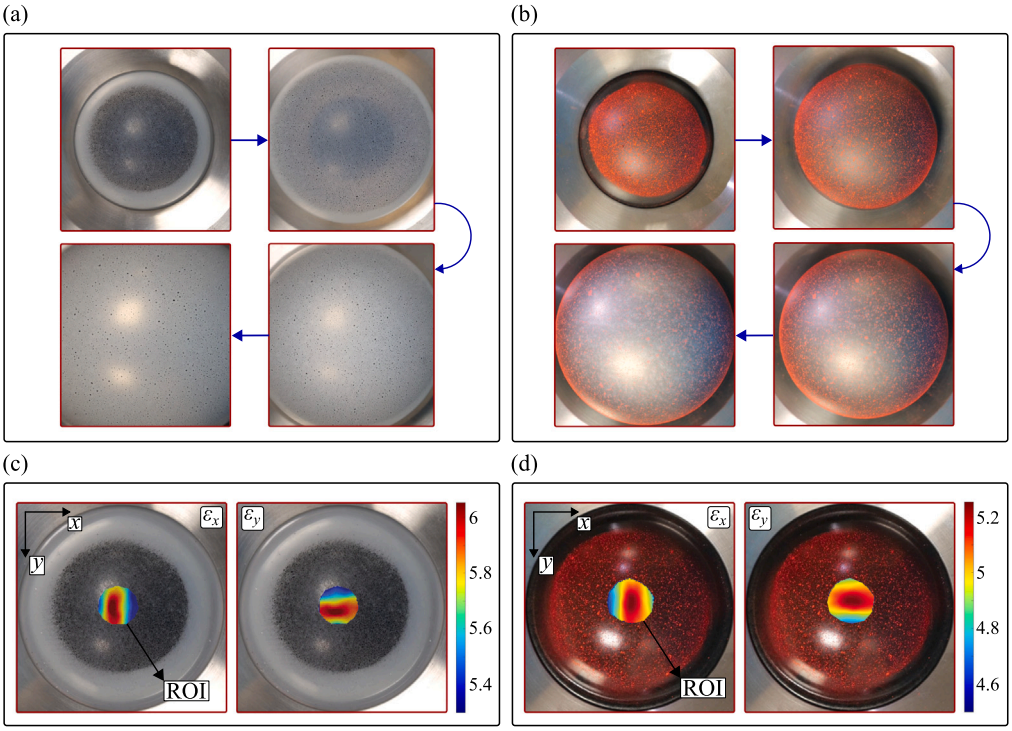

Fig. A.16. DIC analysis using *Ncorr* to determine pole stretch during inflation tests. Figures (a) and (b) show frames extracted by the videos of the tests on silicone membrane and PNC membrane with 2 phr GNP content, respectively. The ROI and contour plots of Green–Lagrange strains ϵ_x and ϵ_y for silicone and PNC membranes are depicted in (c) and (d), respectively.

contribution of the nanofillers compared to the matrix is calculated from Eq. (15) as $\bar{N}/(1-f)$. According to the values in Table C.1, the increases in the elastic modulus are as follows: at 1.4 phr (~0.7% by volume), there is approximately a 55% increase; at 4 phr (~2% by volume), the increase reaches around 220%; and at 10 phr (~5% by volume), the elastic modulus rises by approximately 720%. These substantial enhancements in the elastic modulus, achieved at low volume fractions, underscore the high efficiency of GNP reinforcement.

(2) The intrinsic Young's modulus of GNP nanoparticles is generally estimated to range from 0.5 to 1 TPa, due to factors such as manufacturing imperfections and the number of layers influencing these values. While a simple rule of mixtures could be used to estimate the total composite modulus, it would overestimate the contributions of the nanofillers, as it does not account for stress transfer and interactions between the matrix and nanofillers. In contrast, models like Mori–Tanaka (Shu and Stanciulescu, 2020) and Halpin–Tsai (Wu et al., 2004) incorporate these interactions by applying reduction factors, providing a more accurate estimation of the effective contribution of nanofillers to the elastic modulus. To illustrate this, we apply the Halpin–Tsai model (Wu et al., 2004):

$$E_c = E_m \frac{1+\xi\chi f}{1-\chi f}, \quad \text{with} \quad \chi = \frac{E_n/E_m - 1}{E_n/E_m + \xi} \quad \text{and} \quad \xi = \frac{2w}{t}, \tag{C.1}$$

where E_c is the composite modulus, E_m is the matrix modulus, E_n is the nanoparticle modulus, and w and t represent the width and thickness of the nanoparticles, respectively. According to the data sheet, our GNPs have an approximate width of 7 μm and thickness of 5 nm. However, as observed in the microscopy images (see Appendix A.1), the GNPs tend to interact, stack, and form aggregates, resulting in larger structures composed of several individual particles. For a simplified estimation, it is reasonable to use an approximate value of $w \approx 10$ μm and $t \approx 100$ nm, acknowledging that this is a rough approximation intended for basic computation. Using these values and assuming $E_n = 0.5$ TPa, the elastic modulus values of the nanocomposite calculated from Eq. (C.1) are comparable to those obtained from Eq. (15), with parameters reported in Table C.1. This indicates that the stiffness contributions modeled in our study are generally consistent with established theoretical predictions.

Table C.2
Values of parameters for matrix and nanofiller contributions, W_m and W_n, resulting from fitting to biaxial (inflation) experimental data. Units are in MPa where applicable.

Matrix parameters	Nanofiller parameters				
	GNP content (phr)	α	β	$\bar{N}$	$\bar{\phi}$
A = −0.625	0.2	1.75	1.25	0.088	0.550
	0.4	1.75	1.25	0.223	0.672
B = 0.0516	0.8	1.75	1.25	0.379	0.715
	1.4	1.75	1.25	0.559	0.649
C_{10} = 0.675	2	1.75	1.25	0.754	0.536
	4	1.75	1.25	1.524	0.526
I_m = 4950	6	1.75	1.25	2.234	0.531
	10	1.75	1.25	4.490	0.528

C.2. Membrane inflation

Table C.2 presents the parameters obtained from fitting to biaxial inflation data, as described in Section 5. In this case, the strain energy evaluated at the ultimate stretch of the silicone in the inflation test is $W_{m,u} = 7.817$ MPa.

C.3. Other experimental data

Table C.3 lists the fitting parameters for the matrix contribution, W_m, for datasets 1, 2, and 3, as detailed in Section 6. To simplify the presentation, we do not report all the fitting parameters of the nanofiller contributions, W_n, for all three cases. Instead, we directly

Table C.3
Fitting parameters for the matrix contribution, W_m, derived from modeling the stress–stretch response of experimental data reported in the literature. Units are expressed in MPa.

Dataset	Material	Model	Parameters
Dataset 1, Frogley et al. (2003)	RTV silicone	Mooney–Rivlin with softening	$C_{10} = 0.477$ $C_{01} = -0.411$ $\phi_v = 68.5$
Dataset 2, Young et al. (2018)	TPE	Mooney–Rivlin with softening	$C_{10} = 8.92$ $C_{01} = -7.34$ $\phi_v = 3.33$
Dataset 3, Xing et al. (2014)	NR	Carroll	$A = 0.187$ $B = 1.47 \times 10^{-6}$ $C = 0.464$

report the final values of α and β, and the fitting laws $\bar{N}(f)$ and $\bar{\phi}(f)$, which provide the optimal parameters as functions of the nanofiller content. These are expressed in Eqs. (22)–(24). These laws are referred to the computations of E_m and $W_{m,u}$ described below. Due to the unavailability of detailed stress–stretch data in the small strain regime, as the data were digitized, the estimation of the elastic modulus was based on linearizing each hyperelastic model employed for the matrices. The computed values are as follows:

- *Dataset 1*: $E_m = 6\left(C_{10} + C_{01}\right) = 0.4$ MPa and $W_{m,u} = 7.255$ MPa;
- *Dataset 2*: $E_m = 6\left(C_{10} + C_{01}\right) = 9.465$ MPa and $W_{m,u} = 1.781$ MPa;
- *Dataset 3*: $E_m = 6A + 648B + \sqrt{3}C = 1.927$ MPa and $W_{m,u} = 25.405$ MPa.

The densities of the constituent materials used in the nanocomposites, which are required for calculating the volume fractions (f) for the three referenced datasets, are reported below. Frogley et al. (2003) reported densities of 1.215 g/cm^3 for RTV silicone and 1.34 g/cm^3 for CNTs. For the PNCs by Young et al. (2018), densities are taken as 1.08 g/cm^3 for TPE Alcryn 2265 and 2.2 g/cm^3 for GNPs. Lastly, for the materials from Xing et al. (2014), the densities considered are 0.92 g/cm^3 for NR and 2.2 g/cm^3 for GE.

Appendix D. Numerical solution for the inflation of circular PNC membranes

We consider a circular flat membrane with radius R and thickness H. We define a cylindrical coordinate system (ρ, Θ, Z) with origin in the central point of the membrane. Under the action of pressure p the membrane inflates preserving axisymmetry, with a generic material point $P \equiv (\rho, \Theta, 0)$ moving to $P' \equiv (r, \Theta, z)$. The principal stretches are oriented along the meridians, the latitudinal lines, and the normal to the deformed surface, and are given respectively as follows:

$$\lambda_1 = \sqrt{r'^2 + z'^2}, \quad \lambda_2 = \frac{r}{\rho}, \quad \lambda_3 = \frac{1}{\lambda_1 \lambda_2}, \tag{D.1}$$

where the prime denotes differentiation with respect to ρ. The principal curvatures of the deformed surface are $K_1 = \left(\lambda_1' \eta - \lambda_1 \eta'\right) / \left(\lambda_1^2 \sqrt{\lambda_1^2 - \eta^2}\right)$ and $K_2 = \sqrt{\lambda_1^2 - \eta^2} / \left(\lambda_1 \lambda_2 \rho\right)$, with $\eta = r'$.

For a generic biaxial stress state of an incompressible hyperelastic material described as a function of the first invariant of deformation, $W = W(I_1)$, the principal stress resultants per unit length are given by

$$T_i = 2H w_1 \left(\frac{\lambda_i}{\lambda_j} - \frac{1}{\lambda_i^3 \lambda_j^3}\right), \quad i, j = 1, 2 \tag{D.2}$$

with $w_1 = \partial W / \partial I_1$. The equilibrium equations in radial and normal directions read

$$\begin{aligned} &\frac{dT_1}{dr} + \frac{1}{r}(T_1 - T_2) = 0, \\ &K_1 T_1 + K_2 T_2 = p. \end{aligned} \tag{D.3}$$

Substituting the expressions for T_1, T_2, K_1, and K_2 into Eq. (D.3), the following governing system of differential equations is obtained (Sirotti et al., 2024):

$$\begin{aligned} \lambda_1' &= \frac{\lambda_1 \left[w_1 \left(\eta \lambda_2^4 \lambda_1^2 - 3\eta - \lambda_2^3 \lambda_1^4 + 3\lambda_2\right) - \frac{\partial w_1}{\partial \lambda_2} \lambda_2 \left(\lambda_1^4 \lambda_2^2 - 1\right)\left(\eta - \lambda_2\right)\right]}{\rho \lambda_2 \left[\frac{\partial w_1}{\partial \lambda_1}\left(\lambda_1^5 \lambda_2^2 - \lambda_1\right) + \left(\lambda_2^2 \lambda_1^4 + 3\right) w_1\right]}, \\ \lambda_2' &= \frac{\eta - \lambda_2}{\rho}, \\ \eta' &= \frac{\eta \lambda_1'}{\lambda_1} - \frac{\xi \lambda_1^4 \lambda_2^4 \sqrt{\lambda_1^2 - \eta^2} + 2w_1 \left(\lambda_1^2 \lambda_2^4 - 1\right)\left(\eta^2 - \lambda_1^2\right)}{2\rho w_1 \lambda_2 \left(\lambda_1^4 \lambda_2^2 - 1\right)}, \end{aligned} \tag{D.4}$$

where $\xi = p(\rho/H)$. In the case of the strain energy function proposed in Section 3 for the PNCs, we have $w_1 = (1-f)\partial W_m/\partial I_1 + f \partial W_n / \partial I_1$, with

$$\begin{aligned} \frac{\partial W_m}{\partial I_1} &= A\, e^{-B(I_1 - 3)} + C_{10}\left(1 - \frac{I_1 - 3}{I_m - 3}\right)^{-1}, \\ \frac{\partial W_n}{\partial I_1} &= \frac{\partial W_n}{\partial \psi_n}\frac{\partial \psi_n}{\partial I_1} = \frac{N}{3^\alpha}\alpha\, I_1^{\alpha - 1}\left[1 + \left(\frac{\psi_n}{\phi}\right)^\beta\right]^{-(1+\beta)/\beta}. \end{aligned} \tag{D.5}$$

The derivatives of w_1 with respect to λ_1 and λ_2 are given by

$$\frac{\partial w_1}{\partial \lambda_i} = (1-f)\frac{\partial^2 W_m}{\partial I_1^2}\frac{\partial I_1}{\partial \lambda_i} + f\frac{\partial^2 W_n}{\partial I_1^2}\frac{\partial I_1}{\partial \lambda_i}, \quad i = 1, 2. \tag{D.6}$$

System (D.4) represents an initial value problem that must be integrated along the radius of the membrane, with the additional condition $\lambda_2(L) = 1$ at the outer boundary. Various methods are available for solving the governing ODEs (see, for instance, Verron and Marckmann (2003), Saxena et al. (2019)). We adopted the well-established procedure proposed by Yang and Feng (1970), which offers the advantage of avoiding iterations. The numerical integration was performed in MATLAB using function *ode45*, and the detailed procedure for this solution can be found in Appendix D.1 of Sirotti et al. (2024).

Data availability

Data will be made available on request.

References

Anssari-Benam, A., Bucchi, A., Saccomandi, G., 2021. On the central role of the invariant I_2 in nonlinear elasticity. Internat. J. Engrg. Sci. 163, 103486.
Arash, B., Exner, W., Rolfes, R., 2019. A viscoelastic damage model for nanoparticle/epoxy nanocomposites at finite strain: A multiscale approach. J. Mech. Phys. Solids 128, 162–180.
Barghamadi, M., Ghoreishy, M.H.R., Karrabi, M., Mohammadian-Gezaz, S., 2021. Modeling of nonlinear hyper-viscoelastic and stress softening behaviors of acrylonitrile butadiene rubber/polyvinyl chloride nanocomposites reinforced by nanoclay and graphene. Polym. Compos. 42 (2), 583–596.
Bassyouni, M., Abdel-Aziz, M., Zoromba, M.S., Abdel-Hamid, S., Drioli, E., 2019. A review of polymeric nanocomposite membranes for water purification. J. Ind. Eng. Chem. 73, 19–46.

Caliskan, U., Gulsen, H., 2023. A novel computational multi-scale modeling of randomly-distributed-graphene/epoxy nanocomposites with interfacial interactions. Int. J. Solids Struct. 285, 112553.
Cantournet, S., Boyce, M.C., Tsou, A.H., 2007. Micromechanics and macromechanics of carbon nanotube-enhanced elastomers. J. Mech. Phys. Solids 55 (6), 1321–1339.
Carroll, M.M., 2011. A strain energy function for vulcanized rubbers. J. Elasticity 103, 173–187.
Chen, L., Chen, W., Xue, Y., Zhang, M., Chen, X., Cao, X., Zhang, Z., Li, G., Li, T., 2019. Investigation of the state transition and moving boundary in a pneumatic–hydraulic coupled dielectric elastomer actuator. J. Appl. Mech. 86 (3), 031004.
Cheng, M., Chen, W., 2003. Experimental investigation of the stress–stretch behavior of EPDM rubber with loading rate effects. Int. J. Solids Struct. 40 (18), 4749–4768.
Chieng, B.W., Ibrahim, N.A., Wan Yunus, W.M.Z., Hussein, M.Z., 2013. Poly (lactic acid)/poly (ethylene glycol) polymer nanocomposites: Effects of graphene nanoplatelets. Polymers 6 (1), 93–104.
Choi, J.Y., Zhang, X., Nguyen, H.T., Roenbeck, M.R., Mao, L., Soler-Crespo, R., Nguyen, S.T., Espinosa, H.D., 2021. Atomistic mechanisms of adhesion and shear strength in graphene oxide-polymer interfaces. J. Mech. Phys. Solids 156, 104578.
Corzo, D., Tostado-Blázquez, G., Baran, D., 2020. Flexible electronics: status, challenges and opportunities. Front. Electron. 1, 594003.
Costa, P., Carvalho, M.F., Correia, V., Viana, J.C., Lanceros-Mendez, S., 2018. Polymer nanocomposite-based strain sensors with tailored processability and improved device integration. ACS Appl. Nano Mater. 1 (6), 3015–3025.
Cui, Y., Kundalwal, S.I., Kumar, S., 2016. Gas barrier performance of graphene/polymer nanocomposites. Carbon 98, 313–333.
Dal, H., Açıkgöz, K., Badienia, Y., 2021. On the performance of isotropic hyperelastic constitutive models for rubber-like materials: A state of the art review. Appl. Mech. Rev. 73 (2).
Das, A., Kasaliwal, G.R., Jurk, R., Boldt, R., Fischer, D., Stöckelhuber, K.W., Heinrich, G., 2012. Rubber composites based on graphene nanoplatelets, expanded graphite, carbon nanotubes and their combination: A comparative study. Compos. Sci. Technol. 72 (16), 1961–1967.
Destrade, M., Saccomandi, G., Sgura, I., 2017. Methodical fitting for mathematical models of rubber-like materials. Proc. R. Soc. A: Math. Phys. Eng. Sci. 473 (2198), 20160811.
Du Bois, P.A., Kolling, S., Koesters, M., Frank, T., 2006. Material behaviour of polymers under impact loading. Int. J. Impact Eng. 32 (5), 725–740.
Dufresne, A., Paillet, M., Putaux, J.L., Canet, R., Carmona, F., Delhaes, P., Cui, S., 2002. Processing and characterization of carbon nanotube/poly (styrene-co-butyl acrylate) nanocomposites. J. Mater. Sci. 37, 3915–3923.
Frogley, M.D., Ravich, D., Wagner, H.D., 2003. Mechanical properties of carbon nanoparticle-reinforced elastomers. Compos. Sci. Technol. 63 (11), 1647–1654.
Fu, S., Sun, Z., Huang, P., Li, Y., Hu, N., 2019. Some basic aspects of polymer nanocomposites: A critical review. Nano Mater. Sci. 1 (1), 2–30.
Gao, Y., 2017. Graphene and polymer composites for supercapacitor applications: a review. Nanoscale Res. Lett. 12 (1), 387.
Gasser, T.C., Ogden, R.W., Holzapfel, G.A., 2006. Hyperelastic modelling of arterial layers with distributed collagen fibre orientations. J. R. Soc. Interface 3 (6), 15–35.
Gent, A.N., 1996. A new constitutive relation for rubber. Rubber Chem. Technol. 69 (1), 59–61.
Gorissen, B., Milana, E., Baeyens, A., Broeders, E., Christiaens, J., Collin, K., Reynaerts, D., De Volder, M., 2019. Hardware sequencing of inflatable nonlinear actuators for autonomous soft robots. Adv. Mater. 31 (3), 1804598.
Guimard, N.K., Gomez, N., Schmidt, C.E., 2007. Conducting polymers in biomedical engineering. Prog. Polym. Sci. 32 (8–9), 876–921.
He, H., Zhang, Q., Zhang, Y., Chen, J., Zhang, L., Li, F., 2022. A comparative study of 85 hyperelastic constitutive models for both unfilled rubber and highly filled rubber nanocomposite material. Nano Mater. Sci. 4 (2), 64–82.
Holzapfel, G.A., Gasser, T.C., Ogden, R.W., 2000. A new constitutive framework for arterial wall mechanics and a comparative study of material models. J. Elasticity 61, 1–48.
Idumah, C.I., Obele, C.M., 2021. Understanding interfacial influence on properties of polymer nanocomposites. Surf. Interfaces 22, 100879.
Islam, S., Yang, S., Kim, C.I., 2023. A multiscale continuum model for the mechanics of hyperelastic composite reinforced with nanofibers. Int. J. Solids Struct. 267, 112168.
Itskov, M., 2000. On the theory of fourth-order tensors and their applications in computational mechanics. Comput. Methods Appl. Mech. Engrg. 189 (2), 419–438.
Jouault, N., Dalmas, F., Boué, F., Jestin, J., 2014. Nanoparticles reorganizations in polymer nanocomposites under large deformation. Polymer 55 (10), 2523–2534.
Kim, H., Abdala, A.A., Macosko, C.W., 2010. Graphene/polymer nanocomposites. Macromolecules 43 (16), 6515–6530.
Koerner, H., Liu, W., Alexander, M., Mirau, P., Dowty, H., Vaia, R.A., 2005. Deformation–morphology correlations in electrically conductive carbon nanotube—thermoplastic polyurethane nanocomposites. Polymer 46 (12), 4405–4420.
Kuhl, E., Goriely, A., 2024. I too love I_2: A new class of hyperelastic isotropic incompressible models based solely on the second invariant. J. Mech. Phys. Solids 188, 105670.
Liu, Z., McBride, A., Sharma, B.L., Steinmann, P., Saxena, P., 2021. Coupled electro-elastic deformation and instabilities of a toroidal membrane. J. Mech. Phys. Solids 151, 104221.
Loew, P.J., Peters, B., Beex, L.A., 2019. Rate-dependent phase-field damage modeling of rubber and its experimental parameter identification. J. Mech. Phys. Solids 127, 266–294.
Lopez-Pamies, O., 2010. A new I_1-based hyperelastic model for rubber elastic materials. C. R. Méc. 338 (1), 3–11.
Lorenz, H., Klüppel, M., 2012. Microstructure-based modelling of arbitrary deformation histories of filler-reinforced elastomers. J. Mech. Phys. Solids 60 (11), 1842–1861.
Meunier, L., Chagnon, G., Favier, D., Orgéas, L., Vacher, P., 2008. Mechanical experimental characterisation and numerical modelling of an unfilled silicone rubber. Polym. Test. 27 (6), 765–777.
Miculescu, M., Thakur, V.K., Miculescu, F., Voicu, S.I., 2016. Graphene-based polymer nanocomposite membranes: a review. Polym. Adv. Technol. 27 (7), 844–859.
Molinari, N., Sutton, A., Mostofi, A., 2018. Mechanisms of reinforcement in polymer nanocomposites. Phys. Chem. Chem. Phys. 20 (35), 23085–23094.
Mondal, S., Khastgir, D., 2017. Elastomer reinforcement by graphene nanoplatelets and synergistic improvements of electrical and mechanical properties of composites by hybrid nano fillers of graphene-carbon black & graphene-MWCNT. Composites A 102, 154–165.
Ogden, R.W., 1972. Large deformation isotropic elasticity–on the correlation of theory and experiment for incompressible rubberlike solids. Proc. R. Soc. A 326 (1567), 565–584.
Pelliciari, M., Sirotti, S., Aloisio, A., Tarantino, A.M., 2022. Analytical, numerical and experimental study of the finite inflation of circular membranes. Int. J. Mech. Sci. 226, 107383.
Pelliciari, M., Sirotti, S., Tarantino, A.M., 2023. A strain energy function for large deformations of compressible elastomers. J. Mech. Phys. Solids 176, 105308.
Potts, J.R., Shankar, O., Murali, S., Du, L., Ruoff, R.S., 2013. Latex and two-roll mill processing of thermally-exfoliated graphite oxide/natural rubber nanocomposites. Compos. Sci. Technol. 74, 166–172.
Pucci, E., Saccomandi, G., 2002. A note on the Gent model for rubber-like materials. Rubber Chem. Technol. 75 (5), 839–852.
Qian, D., Dickey, E.C., Andrews, R., Rantell, T., 2000. Load transfer and deformation mechanisms in carbon nanotube-polystyrene composites. Appl. Phys. Lett. 76 (20), 2868–2870.
Qin, Y., Peng, Q., Ding, Y., Lin, Z., Wang, C., Li, Y., Xu, F., Li, J., Yuan, Y., He, X., Li, Y., 2015. Lightweight, superelastic, and mechanically flexible graphene/polyimide nanocomposite foam for strain sensor application. ACS Nano 9 (9), 8933–8941.
Rivlin, R.S., Saunders, D., 1951. Large elastic deformations of isotropic materials VII. Experiments on the deformation of rubber. Philos. Trans. R. Soc. Lond. Ser. A, Math. Phys. Sci. 243 (865), 251–288.
Sadeghpour, E., Guo, Y., Chua, D., Shim, V.P.W., 2020. Dynamic stress–strain response of graphene nanocomposites. Int. J. Impact Eng. 145, 103690.
Saxena, P., Reddy, N.H., Pradhan, S.P., 2019. Magnetoelastic deformation of a circular membrane: wrinkling and limit point instabilities. Int. J. Non-Linear Mech. 116, 250–261.
Senses, E., Akcora, P., 2013. An interface-driven stiffening mechanism in polymer nanocomposites. Macromolecules 46 (5), 1868–1874.
Shen, J., Liu, J., Gao, Y., Li, X., Zhang, L., 2014. Elucidating and tuning the strain-induced non-linear behavior of polymer nanocomposites: a detailed molecular dynamics simulation study. Soft Matter 10 (28), 5099–5113.
Shin, H., Choi, J., Cho, M., 2019. An efficient multiscale homogenization modeling approach to describe hyperelastic behavior of polymer nanocomposites. Compos. Sci. Technol. 175, 128–134.
Shu, W., Stanciulescu, I., 2020. Multiscale homogenization method for the prediction of elastic properties of fiber-reinforced composites. Int. J. Solids Struct. 203, 249–263.
Sirotti, S., Pelliciari, M., Tarantino, A.M., 2024. Effect of compressibility on the mechanics of hyperelastic membranes. Int. J. Mech. Sci. 109441.
Stewart, B.G., Sitaraman, S.K., 2021. Biaxial inflation stretch test for flexible electronics. Adv. Eng. Mater. 2001503.
Thakur, V.K., Kessler, M.R., 2015. Self-healing polymer nanocomposite materials: A review. Polymer 69, 369–383.
Tomita, Y., Azuma, K., Naito, M., 2008. Computational evaluation of strain-rate-dependent deformation behavior of rubber and carbon-black-filled rubber under monotonic and cyclic straining. Int. J. Mech. Sci. 50 (5), 856–868.
Varol, H.S., Meng, F., Hosseinkhani, B., Malm, C., Bonn, D., Bonn, M., Zaccone, A., Parekh, S.H., 2017. Nanoparticle amount, and not size, determines chain alignment and nonlinear hardening in polymer nanocomposites. Proc. Natl. Acad. Sci. 114 (16), E3170–E3177.
Venkata, S.P., Balbi, V., Destrade, M., Zurlo, G., 2024. Designing necks and wrinkles in inflated auxetic membranes. Int. J. Mech. Sci. 268, 109031.
Verron, E., Marckmann, G., 2003. Inflation of elastomeric circular membranes using network constitutive equations. Int. J. Non-Linear Mech. 38 (8), 1221–1235.
Volokh, K.Y., 2007. Hyperelasticity with softening for modeling materials failure. J. Mech. Phys. Solids 55 (10), 2237–2264.
Volokh, K.Y., 2010. On modeling failure of rubber-like materials. Mech. Res. Commun. 37 (8), 684–689.
Wang, F., Drzal, L.T., Qin, Y., Huang, Z., 2015. Mechanical properties and thermal conductivity of graphene nanoplatelet/epoxy composites. J. Mater. Sci. 50, 1082–1093.

Wang, J., Gong, L., Xi, S., Li, C., Su, Y., Yang, L., 2024. Synergistic effect of interface and agglomeration on Young's modulus of graphene-polymer nanocomposites. Int. J. Solids Struct. 292, 112716.

Wang, Q., Zhu, L., 2011. Polymer nanocomposites for electrical energy storage. J. Polym. Sci B: Polym. Phys. 49 (20), 1421–1429.

Winey, K.I., Kashiwagi, T., Mu, M., 2007. Improving electrical conductivity and thermal properties of polymers by the addition of carbon nanotubes as fillers. MRS Bull. 32 (4), 348–353.

Wu, Y.P., Jia, Q.X., Yu, D.S., Zhang, L.Q., 2004. Modeling Young's modulus of rubber–clay nanocomposites using composite theories. Polym. Test. 23 (8), 903–909.

Xing, W., Wu, J., Huang, G., Li, H., Tang, M., Fu, X., 2014. Enhanced mechanical properties of graphene/natural rubber nanocomposites at low content. Polym. Int. 63 (9), 1674–1681.

Xu, J., Wu, H.C., Zhu, C., Ehrlich, A., Shaw, L., Nikolka, M., Wang, S., Molina-Lopez, F., Gu, X., Luo, S., et al., 2019. Multi-scale ordering in highly stretchable polymer semiconducting films. Nature Mater. 18 (6), 594–601.

Yamaguchi, K., Busfield, J.J.C., Thomas, A.G., 2003. Electrical and mechanical behavior of filled elastomers. I. The effect of strain. J. Polym. Sci B: Polym. Phys. 41 (17), 2079–2089.

Yang, W.H., Feng, W.W., 1970. On axisymmetrical deformations of nonlinear membranes. J. Appl. Mech. 37 (4), 1002–1011.

Yang, H., Yao, X., Zheng, Z., Gong, L., Yuan, L., Yuan, Y., Liu, Y., 2018. Highly sensitive and stretchable graphene-silicone rubber composites for strain sensing. Compos. Sci. Technol. 167, 371–378.

Yeoh, O.H., 1990. Characterization of elastic properties of carbon-black-filled rubber vulcanizates. Rubber Chem. Technol. 63 (5), 792–805.

Yeoh, O.H., Fleming, P.D., 1997. A new attempt to reconcile the statistical and phenomenological theories of rubber elasticity. J. Polym. Sci B: Polym. Phys. 35 (12), 1919–1931.

Young, R.J., Liu, M., Kinloch, I.A., Li, S., Zhao, X., Vallés, C., Papageorgiou, D.G., 2018. The mechanics of reinforcement of polymers by graphene nanoplatelets. Compos. Sci. Technol. 154, 110–116.

Zare, Y., 2016a. Modeling the strength and thickness of the interphase in polymer nanocomposite reinforced with spherical nanoparticles by a coupling methodology. J. Colloid Interface Sci. 465, 342–346.

Zare, Y., 2016b. Study of nanoparticles aggregation/agglomeration in polymer particulate nanocomposites by mechanical properties. Composites A 84, 158–164.